



Cite this: *Phys. Chem. Chem. Phys.*,
2024, 26, 11243

Progress on enhancing the charge separation efficiency of carbon nitride for robust photocatalytic H₂ production

Mengmeng Shao, ^a Yangfan Shao ^b and Hui Pan ^{*cd}

Solar-driven H₂ production from water splitting with efficient photocatalysts is a sustainable strategy to meet the clean energy demand and alleviate the approaching environmental issues caused by fossil fuel consumption. Among various semiconductor-based photocatalysts, graphitic carbon nitride (g-C₃N₄) has attracted much attention due to its advantages of long term-stability, visible light response, low cost, and easy preparation. However, the intrinsic Coulombic attraction between charge carriers and the interlayer electrostatic barrier of bulk g-C₃N₄ result in severe charge recombination and low charge separation efficiency. This perspective summarizes the recent progress in the development of g-C₃N₄ photocatalytic systems, and focuses on three main modification strategies for promoting charge transfer and minimizing charge recombination, including structural modulation, heterojunction construction, and cocatalyst loading. Based on this progress, we provide conclusions regarding the current challenges of further improving photocatalytic efficiency to fulfill commercial requirements, and propose some recommendations for the design of novel and satisfactory g-C₃N₄ photocatalysts, which is expected to progress the solar-to-hydrogen conversion.

Received 30th December 2023,
Accepted 17th March 2024

DOI: 10.1039/d3cp06333j

rsc.li/pccp

1. Introduction

Fuel is an indispensable driving force for the development of human society. In the ancient world, humans bade farewell to a life of devouring raw meat by drilling wood to make fire, and began the era of using firewood as the main energy source. Since the 18th century, with the outbreak of the industrial revolution, fossil fuels, such as coal, oil, and natural gas, have emerged as the main energy source in the world. Nowadays the increasing demand for fossil fuels and various environmental issues (e.g., global warming, acid rain, and smog) caused by their excessive consumption have posed great challenges to the current energy system. Among emerging energy sources, hydrogen has the highest energy density, is eco-friendly, abundant, and carbon-neutral, and is considered a promising alternative to fossil fuels.^{1,2}

In recent decades, solar-driven H₂ production from water splitting has received great attention due to the green process only involving sustainable solar energy, water, and photocatalysts.^{3–5}

Starting from the pioneering work of Fujishima and Honda about water-splitting on TiO₂,⁶ numerous active semiconductor photocatalysts have been developed, such as CdS, g-C₃N₄, BiOBr, Cd_xZn_{1-x}S, GaN-ZnO solid solution, and ZnIn₂S₄.^{7–17} The typical process of photocatalytic water-splitting mainly includes three steps (Fig. 1a):^{18,19} (1) the generation of photo-induced electron and hole pairs, where the electrons in the valence band (VB) are excited to the conduction band (CB) under light irradiation with higher energy than the band gap of photocatalysts; (2) the separation and transfer of photo-induced charge carriers, which are always accompanied by recombination; (3) the transferred charges participate in the surface catalytic reaction, producing H₂ and O₂ by H⁺ reduction and H₂O oxidation, where the redox potentials of H⁺/H₂ and O₂/H₂O should be located between the CB minimum and VB maximum. Based on the above steps, the development of robust photocatalysts is focused on increasing the light-harvesting range, improving charge separation efficiency, and accelerating surface redox reactions. Currently, to promote the practical application of photocatalytic H₂ production, the photocatalysts with the visible light response and high apparent quantum efficiency (AQE) attain significant interest.

As reported, the polymeric semiconductor, graphitic carbon nitride (g-C₃N₄), is well known as a photocatalyst for H₂ production because of its advantageous layered structure, long-term stability, ease of synthesis, low cost, and eco-friendly nature. Especially, g-C₃N₄ with a narrow band gap

^a School of Materials Science and Engineering, Dongguan University of Technology, Dongguan 523808, China. E-mail: shaomm@dgut.edu.cn

^b Institute of Materials Research, Tsinghua Shenzhen International Graduate School, Tsinghua University, Shenzhen 518055, China

^c Institute of Applied Physics and Materials Engineering, University of Macau, Macao 999078, China. E-mail: huipan@um.edu.mo

^d Department of Physics and Chemistry, Faculty of Science and Technology, University of Macau, Macao 999078, China

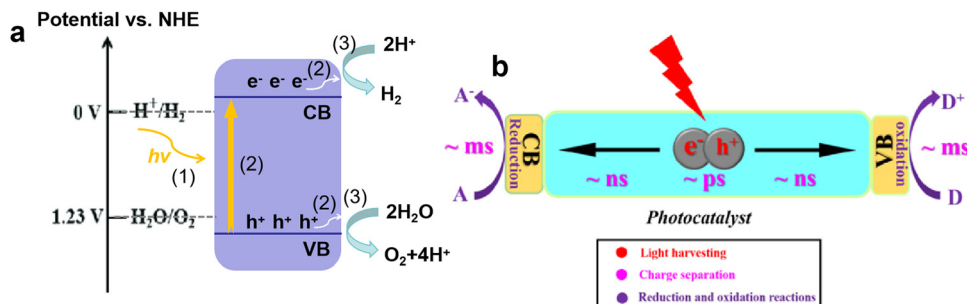


Fig. 1 Photocatalytic H₂ evolution process (a). The kinetic times for separation, transfer, and reaction of photogenerated charge carriers (b). Reproduced with permission from ref. 31. Copyright 2021, Wiley-VCH.

(~2.7 eV) is capable of harvesting visible light, and its band edge positions are suitable for water splitting.^{20–22} In 2009, Wang *et al.*²³ first showed photocatalytic H₂ production from water using g-C₃N₄ as the photocatalyst under visible light irradiation. The result of Wang's study motivated the researchers to further explore and improve the photocatalytic H₂ production performance of g-C₃N₄. For instance, Zhu and Zhang *et al.*²⁴ prepared 3D porous g-C₃N₄ through a bottom-up self-assembly method, achieving photocatalytic overall water splitting with ~1.4% AQE at 420 nm. Liu and Lu *et al.*²⁵ designed a ZnIn₂S₄/g-C₃N₄ heterojunction composite, which displayed excellent photocatalytic activity with a H₂ production rate of about 87 μmol h⁻¹ and AQE of 10.74% at 420 nm. Our group also explored the photocatalytic performance of different cocatalyst loaded g-C₃N₄,^{26–28} and found the H₂ production rates of VS₂/g-C₃N₄ and W₂C/g-C₃N₄ both exceeded 80 μmol h⁻¹, while the highest quantum efficiency achieved on VS₂/g-C₃N₄ was just 5.5%.

However, although g-C₃N₄ is a very promising photocatalyst for H₂ production from water splitting, and related studies have made some progress, the quantum efficiency is still too low to meet the solar-to-hydrogen conversion efficiency of 10% required for commercialization. The main reason lies in the high recombination rate of photo-induced charges, leading to less electron involvement in the H₂ evolution reaction.^{29,30} For photocatalysis, “no charge, no reaction” is clear, the charge separation and transfer are crucial for photocatalytic performance. As shown in Fig. 1b, due to the strong Coulombic interaction between electron and hole pairs, the charge carriers undergo severe recombination within the bulk and surface phases (several ps < t < dozens ps), which is faster than the separation of these charges (~ns) and the involved surface reactions (~ms).^{31,32} Another challenge for charge separation and transfer is the existence of the interlayer electrostatic barrier in bulk g-C₃N₄, which hinders the transfer of electrons from the bulk to surface active sites, and results in severe bulk recombination and poor photocatalytic activity.^{33,34} Thus, the efficient charge separation and opposite transfer to surface redox sites are of the utmost importance in photocatalytic reactions.

During the last decade, a series of papers have been published revealing the advances in the field of photocatalytic H₂ production over g-C₃N₄.^{35–37} As we know, the separation and transfer of charges is a crucial step for photocatalysis.

Currently, various approaches have been developed to modify g-C₃N₄ and improve charge separation efficiency, such as morphological control, metal/non-metal doping, heterojunction, etc.²² Considering the unique characteristics of each strategy, it is necessary to compare different modification methods and summarize their advantages in a review, which is beneficial for further understanding the mechanism of charge separation and transfer, providing strategies for developing highly active g-C₃N₄-based photocatalysts for H₂ production.

Therefore, in this perspective, following the introduction, our focus is to discuss the general strategies for strengthening charge separation and transfer in g-C₃N₄, and analyze their respective characteristics. We then extend our discussion to the synergistic effect of combining multiple methods on the improvement of photocatalytic efficiency. Finally, we conclude with some recommendations for the design of benchmark g-C₃N₄-based photocatalysts for practical applications.

2. Structural modulation of g-C₃N₄

As discussed in the introduction, the poor charge separation efficiency of photocatalysts essentially lies in the high Coulombic attraction of photo-induced charges, which makes the dissociation of electron and hole pairs into free charges difficult. For the g-C₃N₄ photocatalyst, another added problem is the presence of electrostatic barriers between layers, which results in the trapping of charge carriers in the bulk phase and few electrons being transferred to the surface. Thus, to facilitate charge separation and transfer in g-C₃N₄, the modulation of intrinsic structure is a commonly adopted strategy. In this section, we focus on discussing several important published studies about structural modulation of g-C₃N₄ via crystal structure regulation, morphological tuning and doping engineering. A comparison of the photocatalytic H₂ evolution activity of the recent g-C₃N₄ systems based on structural modulation is given in Table 1.

2.1. Crystal structure regulation

g-C₃N₄ is typically synthesized through the traditional thermal polymerization of organic compounds, such as melamine, dicyandiamide, urea, thiourea, etc.³⁸ The simple one-step polymerization method often causes incomplete polycondensation,

Table 1 Photocatalytic H_2 evolution activity of recent $g\text{-}C_3N_4$ systems based on structural modulation

| Photocatalyst | Light source | Reaction conditions | H_2 evolution rate | AQE | Ref. |
|--|--|--|--------------------------------------|------------------|------|
| Crystalline $g\text{-}C_3N_4$ nanosheets | 300 W Xe lamp ($\lambda > 420$ nm) | 25 mg catalyst, TEOA ^g solution, Pt cocatalyst | 20.9 mmol $h^{-1} g^{-1}$ | 73.6% at 420 nm | 44 |
| Single-crystalline PTI ^g nanosheets | 300 W Xe lamp ($\lambda > 300$ nm) | 100 mg catalyst, pure water, CoO_x and $PtCrO_x$ cocatalysts | 6100 $\mu\text{mol} h^{-1} g^{-1}$ | 25% at 365 nm | 45 |
| CN-TM ^b | 300 W Xe lamp ($\lambda > 420$ nm) | 50 mg catalyst, TEOA solution, Pt cocatalyst | 31.35 $\mu\text{mol} h^{-1} g^{-1}$ | 21.03% at 420 nm | 47 |
| Prism-like PTI | 300 W Xe lamp ($\lambda > 300$ nm) | 100 mg catalyst, pure water, Pt/Co cocatalysts | 1890 $\mu\text{mol} h^{-1} g^{-1}$ | 8% at 365 nm | 48 |
| $g\text{-}C_3N_4$ nanosheets | 300 W Xe lamp ($\lambda > 400$ nm) | 50 mg catalyst, TEOA solution, Pt cocatalyst | 10.14 mmol $h^{-1} g^{-1}$ | 7.34% at 400 nm | 49 |
| $g\text{-}C_3N_4$ nanosheets | 300 W Xe lamp ($\lambda > 400$ nm) | 20 mg catalyst, TEOA solution, Pt cocatalyst | 2590 $\mu\text{mol} h^{-1} g^{-1}$ | 10.4% at 400 nm | 50 |
| $g\text{-}C_3N_4$ nanorods | 300 W Xe lamp ($\lambda > 420$ nm) | 10 mg catalyst, TEOA solution, Pt cocatalyst | 578.5 $\mu\text{mol} h^{-1} g^{-1}$ | — | 54 |
| $g\text{-}C_3N_4$ nanorods | 300 W Xe lamp ($\lambda > 420$ nm) | 25 mg catalyst, TEOA solution, Pt cocatalyst | 732.0 $\mu\text{mol} h^{-1} g^{-1}$ | 7.1% at 420 nm | 56 |
| $g\text{-}C_3N_4$ nanotubes | 300 W Xe lamp ($\lambda > 420$ nm) | 20 mg catalyst, TEOA solution, Pt cocatalyst | 4779.8 $\mu\text{mol} h^{-1} g^{-1}$ | — | 60 |
| $g\text{-}C_3N_4$ tubes | 350 W Xe lamp | 30 mg catalyst, TEOA solution, Ni_2P cocatalyst | 19.25 mmol $h^{-1} g^{-1}$ | 5.8% at 400 nm | 62 |
| C_3N_4 -TDA ^c | 300 W Xe lamp ($\lambda > 420$ nm) | 20 mg catalyst, TEOA solution, Pt cocatalyst | 12.35 mmol $h^{-1} g^{-1}$ | 40.5% at 400 nm | 69 |
| $g\text{-}C_3N_3$ | 350 W Xe lamp | 50 mg catalyst, $Na_2SnNa_2SO_3$ solution | 14.9 mmol $h^{-1} g^{-1}$ | 19.9% at 420 nm | 70 |
| Xe lamp AM1.5 ($\lambda > 420$ nm) | 50 mg catalyst, TEOA solution, Pt cocatalyst | 10.8 mmol $h^{-1} g^{-1}$ | 3.35% at 420 nm | 71 | |
| $Ar^d\text{-}C_3N_4$ | 50 W LED ($\lambda > 420$ nm) | 50 mg catalyst, TEOA and K_2HPO_4 solution, Pt cocatalyst | 13 mmol $h^{-1} g^{-1}$ | 65% at 420 nm | 73 |
| CN-ATZ-NaCl ^e | 300 W Xe lamp | 50 mg catalyst, TEOA solution, Pt cocatalyst | 4240 $\mu\text{mol} h^{-1} g^{-1}$ | 12% at 420 nm | 74 |
| PHIA ^f | 350 W Xe lamp | 30 mg catalyst, TEOA solution | 14 mmol $h^{-1} g^{-1}$ | 22.9% at 420 nm | 78 |
| Li- $g\text{-}C_3N_4$ | 300 W Xe lamp ($\lambda > 420$ nm) | 100 mg catalyst, TEOA solution, Pt cocatalyst | 1.35 mmol $h^{-1} g^{-1}$ | — | 80 |
| In- $g\text{-}C_3N_4$ | 300 W Xe lamp ($\lambda > 420$ nm) | 20 mg catalyst, methanol solution, Pt cocatalyst | 10.6 nmol $h^{-1} g^{-1}$ | 9.2% at 420 nm | 81 |

^a Poly(triazine imide) (PTI) based carbon nitride. ^b The precursors of thiourea (T) and melamine (M) for $g\text{-}C_3N_4$ (CN). ^c Thiophene-2,5-dicarbaldehyde (TDA). ^d Aromatized terminal. ^e Aminated tetrazole (ATZ) is used to prepare $g\text{-}C_3N_4$ in NaCl/KCl molten salt. ^f The precursor of 2-aminothiophene-3-carbonitrile (A) for poly-heptazine-imide (PHI) based carbon nitride. ^g Triethanolamine.

a low degree of polymerization, and poor crystallinity of $g\text{-}C_3N_4$, which bring about many internal and surface defects, thereby increasing the charge recombination centers and resulting in poor photocatalytic activity (Fig. 2).^{39,40} Therefore, it is necessary to prepare highly crystalline $g\text{-}C_3N_4$ with less defects for enhanced charge separation efficiency and efficient photocatalytic reaction.

Many strategies have been developed to promote the polymerization of precursors and synthesize the highly crystalline $g\text{-}C_3N_4$, including salt-assisted methods, microwave synthesis, two-step calcination, etc.⁴¹⁻⁴³ For example, Song *et al.*⁴⁴ first prepared ultrathin $g\text{-}C_3N_4$ nanosheets by air-assisted thermal exfoliation, then the resulting nanosheets were treated in the NaCl/KCl molten salts to obtain the highly crystalline $g\text{-}C_3N_4$ nanosheets based on the heptazine-triazine units (donor-acceptor motifs, D-A). The high crystallinity and formed D-A structure promoted charge separation and transfer, resulting in a much higher H_2 evolution activity of 20.9 mmol $h^{-1} g^{-1}$ with an AQE of 73.6% at 420 nm compared with the original $g\text{-}C_3N_4$ nanosheets (1.0 mmol $h^{-1} g^{-1}$). Wang and co-workers synthesized a single-crystalline carbon nitride, poly(triazine imide) nanosheets (PTI), through ternary molten salt treatment (LiCl/KCl/NaCl).⁴⁵ Compared to binary molten salt systems (LiCl/KCl or NaCl/LiCl), the ternary eutectic salts could provide a more mild polymerization environment with higher melting points, which was beneficial to the in-plane polymerization and extension of the conjugated structure, leading to the formation of single-crystalline PTI nanosheets with less structure defects and a shorter charge migration distance. Thus, the obtained PTI nanosheets exhibited a high photocatalytic activity with an AQE of 25% at 365 nm for overall water splitting. In addition, compared with the traditional calcination process, the microwave method can quickly increase the temperature and trigger strong collisions between the reactants, thereby promoting the polymerization reaction and resulting in highly crystalline and active $g\text{-}C_3N_4$.⁴⁶ Chen and Yang *et al.*⁴⁷ combined the molten-

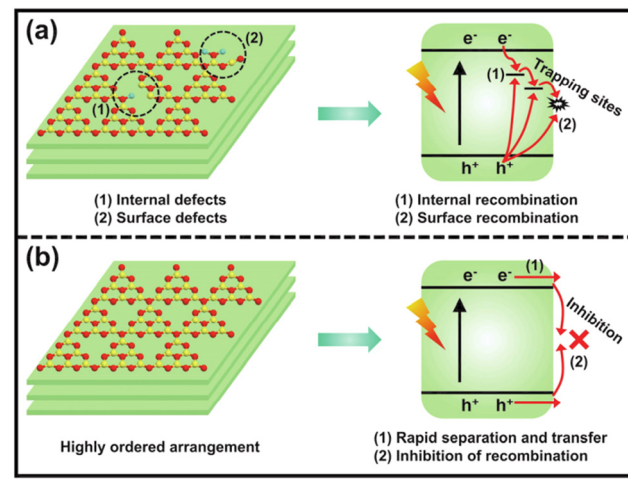


Fig. 2 The charge separation and transfer of conventional poorly-crystalline $g\text{-}C_3N_4$ (a) and highly ordered $g\text{-}C_3N_4$ (b). Reproduced with permission from ref. 39. Copyright 2023, Elsevier.

salt strategy and microwave method to prepare highly active triazine-heptazine-based $\text{g-C}_3\text{N}_4$ with a H_2 evolution rate of $3135 \mu\text{mol h}^{-1} \text{g}^{-1}$ (AQE of 21.03% at 420 nm), which was obviously higher than that of $\text{g-C}_3\text{N}_4$ treated with traditional high-temperature calcination ($2591 \mu\text{mol h}^{-1} \text{g}^{-1}$).

Apart from crystallinity regulation, recently, Wang and co-workers investigated the influence of crystal planes on photocatalytic water splitting.⁴⁸ They prepared the highly crystalline poly-triazine imides-based carbon nitride (PTI) with a prism-like shape and different facets *via* the KCl/LiCl molten salt-assisted method. The results of *in-situ* photodeposition of the Pt cocatalyst demonstrated that the prismatic planes (1010) were the main reactive facets for catalytic reaction, as the Pt cocatalyst tended to accumulate on the (1010) planes. Furthermore, the calculation results also indicated that the electrons could easily transfer toward the prismatic (1010) planes. Based on this discovery, PTI catalysts with different surface area ratios of the (1010) planes were designed, and it was found that the photocatalytic activity increased with the increasing surface area ratio of the (1010) planes, and the optimal AQE of overall water splitting reached 8% at 365 nm with a H_2 evolution rate of $1890 \mu\text{mol h}^{-1} \text{g}^{-1}$. Thus, the development of the crystalline $\text{g-C}_3\text{N}_4$ -based system with less internal defects and more reactive facets exposed can improve charge separation efficiency and achieve the desired photocatalytic activity.

2.2. Morphological tuning

For the severe charge recombination in bulk $\text{g-C}_3\text{N}_4$, the design of ultrathin $\text{g-C}_3\text{N}_4$ nanosheets with expanded layer spacing is

an effective method to weaken or break the shackle of interlayer electrostatic barriers and promote electron transfer from the bulk to the surface. For example, Yang and Kong *et al.*⁴⁹ prepared a series of porous $\text{g-C}_3\text{N}_4$ nanosheets with different thicknesses (2–20 nm) through a thermal-triggering *in-situ* gas-shocking method. The most exfoliated $\text{g-C}_3\text{N}_4$ nanosheets presented an ultrathin structure with only 2 nm thickness, resulting in a larger interlayer spacing. The results showed that the ultrathin $\text{g-C}_3\text{N}_4$ nanosheets (~ 2 nm) exhibited the highest photocatalytic activity with a H_2 production rate up to $10.14 \text{ mmol h}^{-1} \text{g}^{-1}$ (AQE of 7.34% at 400 nm), which was about 57 times that of bulk $\text{g-C}_3\text{N}_4$. The obviously enhanced photocatalytic activity was attributed to the fact that the ultrathin structure not only weakens the interlayer electrostatic barrier and promotes charge transfer to the surface, but also shortens the charge migration distance, thereby achieving a high charge separation efficiency. Shi *et al.*⁵⁰ also reported the significantly improved photocatalytic H_2 production activity over $\text{g-C}_3\text{N}_4$ nanosheets. They developed an available bottom-up acidification method to prepare the ultrathin $\text{g-C}_3\text{N}_4$ nanosheets with an average thickness of ~ 3 nm (Fig. 3a–d). As a result, the as-prepared $\text{g-C}_3\text{N}_4$ nanosheets not only showed a high AQE at 400 nm (10.4%) and 420 nm (8.4%), but also exhibited an enhanced photocatalytic H_2 evolution rate of $2590 \mu\text{mol h}^{-1} \text{g}^{-1}$, which was nearly 10-fold higher than that of bulk $\text{g-C}_3\text{N}_4$. The combined characterizations of electrochemical impedance spectra (EIS), photocurrent responses, and time-resolved PL spectra clearly demonstrated that the

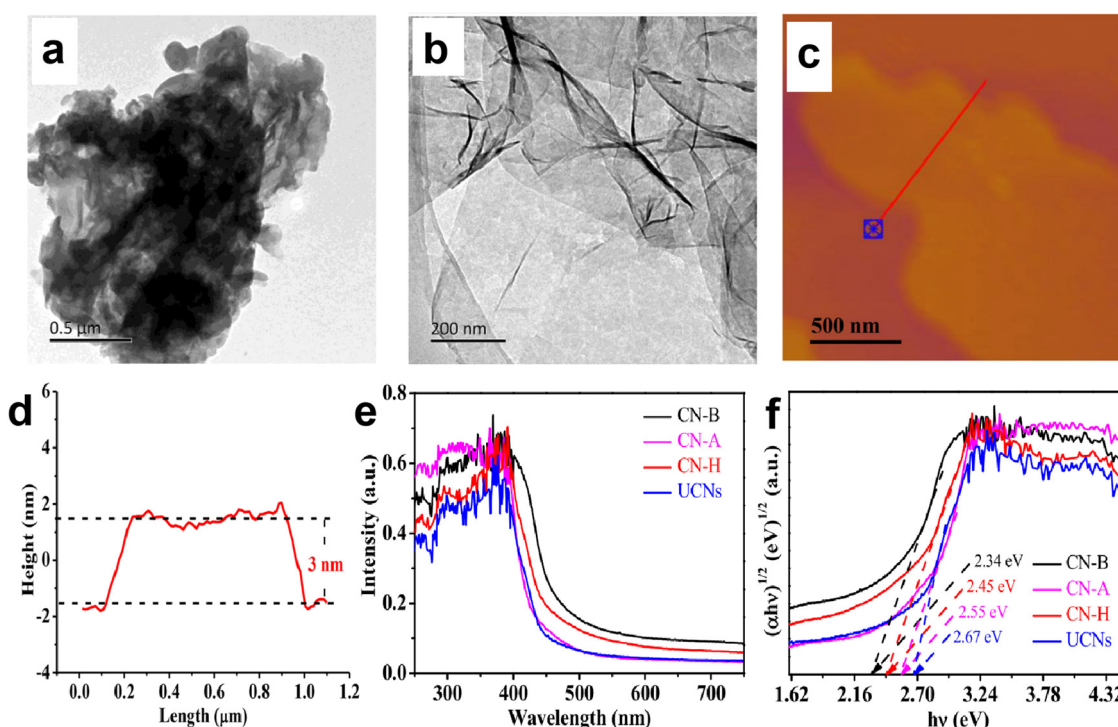


Fig. 3 TEM images of bulk $\text{g-C}_3\text{N}_4$ (a) and ultrathin $\text{g-C}_3\text{N}_4$ nanosheets (b). AFM image of $\text{g-C}_3\text{N}_4$ nanosheets (c) and the corresponding height curves determined along the red line (d). UV-vis absorption spectra (e) and Tauc plots of the as-prepared $\text{g-C}_3\text{N}_4$ materials (f), where CN-B and UCNs correspond to bulk $\text{g-C}_3\text{N}_4$ and ultrathin $\text{g-C}_3\text{N}_4$ nanosheets, respectively. Reproduced with permission from ref. 50. Copyright 2020, Elsevier.

excellent photocatalytic activity of $\text{g-C}_3\text{N}_4$ nanosheets was due to the improved charge transfer and separation as well as the prolonged charge lifetime.

Although the nanosheet structure can effectively reduce the charge recombination in the bulk phase of $\text{g-C}_3\text{N}_4$, and shorten the charge migration path to facilitate the subsequent catalytic reaction, the quantum confinement effect of nanoscale $\text{g-C}_3\text{N}_4$ can lead to an increase in its bandgap, which weakens the visible light response ability of $\text{g-C}_3\text{N}_4$ and limits the improvement of photocatalytic performance.^{50–52} For instance, the light absorption edges of the $\text{g-C}_3\text{N}_4$ nanosheets prepared by Shi *et al.*⁵⁰ displayed a blue shift (Fig. 3e and f), implying the decreased light absorption range and enlarged bandgap of nanoscale $\text{g-C}_3\text{N}_4$. The corresponding Tauc plots clearly showed that the bandgap of the nanosheet structure (2.67 eV) was larger than that of the bulk structure (2.34 eV).

In addition to 2D nanosheet structures, 1D $\text{g-C}_3\text{N}_4$ nanorods or nanotubes have also received extensive attention due to their structural advantages in facilitating charge transfer along the axis.^{53–55} Zhu's group developed a network structure assembled by $\text{g-C}_3\text{N}_4$ nanorods for H_2 evolution and phenol degradation.⁵⁴ The higher intensity of photocurrent response and smaller arc radius in the Nyquist plots of the $\text{g-C}_3\text{N}_4$ nanorod network determined the obviously enhanced charge separation and transfer efficiency. Thus, compared to bulk $\text{g-C}_3\text{N}_4$, the $\text{g-C}_3\text{N}_4$ nanorod

system displayed higher photocatalytic activity with a H_2 evolution rate of $578.5 \mu\text{mol h}^{-1} \text{g}^{-1}$, a nearly six-fold increase. Liu *et al.*⁵⁶ prepared the oxygen doped porous $\text{g-C}_3\text{N}_4$ nanorods, and found that the obtained $\text{g-C}_3\text{N}_4$ nanorods with Pt loading displayed an excellent photocatalytic H_2 evolution rate of $732 \mu\text{mol h}^{-1} \text{g}^{-1}$, nearly 6 times higher than the bulk $\text{g-C}_3\text{N}_4$ system. Furthermore, an AQE of 7.1% was achieved at 420 nm in TEOA solution, 0.29% in pure water. Compared with $\text{g-C}_3\text{N}_4$ nanorods, the nanotubes not only have the advantages of a 1D structure, but also promote the directional migration of photo-induced electrons from concave to convex due to the formation of apparent potential difference between the inner and outer surface of the tubular structure.^{57–59} Meanwhile, the hollow tubular structure can enhance light scattering and improve the light response of $\text{g-C}_3\text{N}_4$ nanotubes.^{60,61} For example, Song *et al.*⁶² prepared $\text{g-C}_3\text{N}_4$ square tubes and loaded Ni_2P as a cocatalyst on the surface of the $\text{g-C}_3\text{N}_4$ tubes (Fig. 4). The calculation and characterization results confirmed the directional electron transfer from the inner to the outer surface of the $\text{g-C}_3\text{N}_4$ tubes, and the increased light response range. Thus, the photocatalytic H_2 evolution activity of the Ni_2P loaded $\text{g-C}_3\text{N}_4$ tube was much higher than that of pristine $\text{g-C}_3\text{N}_4$ supported with noble metals.

2.3. Doping engineering

Doping engineering is another general strategy for regulating the intrinsic structure of $\text{g-C}_3\text{N}_4$. The incorporation of

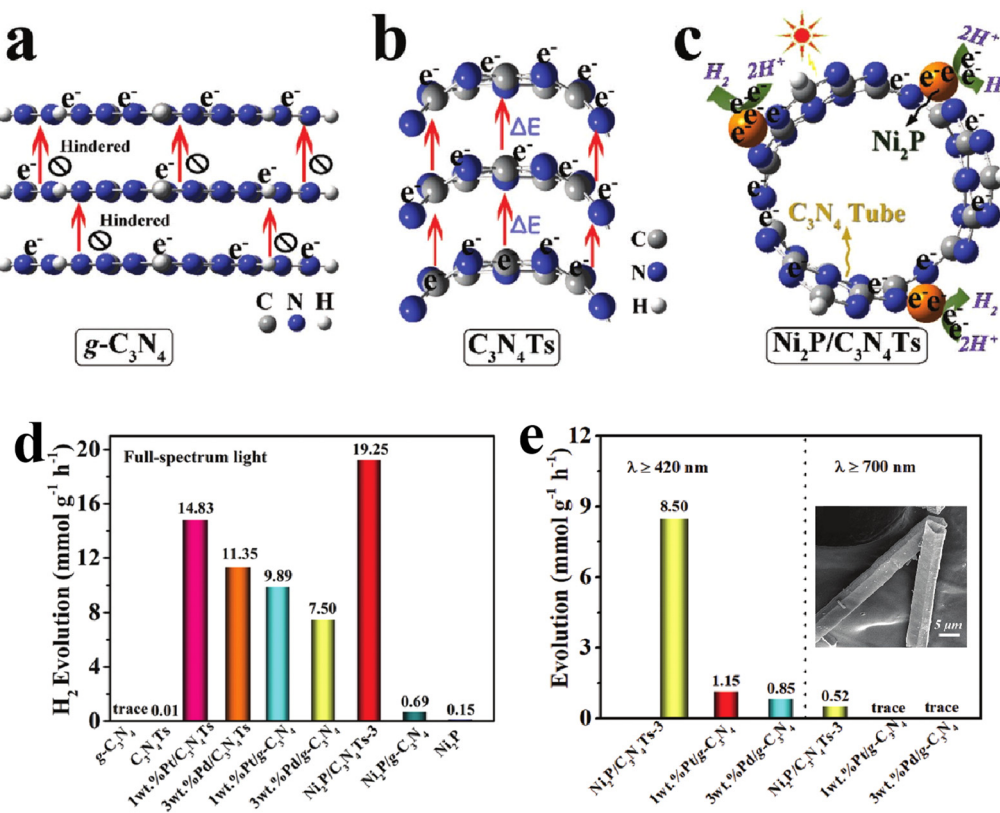


Fig. 4 Schematic illustration of spatial separation and utilization of photo-induced electrons in bulk $\text{g-C}_3\text{N}_4$ (a), $\text{g-C}_3\text{N}_4$ tube (b), and $\text{Ni}_2\text{P}/\text{g-C}_3\text{N}_4$ tube (c); photocatalytic H_2 evolution activities at different wavelengths for bulk $\text{g-C}_3\text{N}_4$ and $\text{g-C}_3\text{N}_4$ tube systems (d) and (e); the inset of (e) is a FESEM image of the $\text{g-C}_3\text{N}_4$ tube. Reproduced with permission from ref. 42. Copyright 2020, Wiley-VCH.

heteroatoms in g-C₃N₄ or grafting other delocalization groups would damage the planar π -conjugated structure and lead to differentiation of delocalized π -electron distribution, thereby promoting the directional transfer of photogenerated charges along the potential difference.^{63,64} Based on the typical 2D stacking structure of g-C₃N₄, there are two main doping configurations, in-plane doping and interlayer doping.

It is known that the high geometrical symmetry of the planar tri-*s*-triazine structure of g-C₃N₄ brings about the uniform π -electron distribution,⁶⁵ which results in random charge transfer within the plane. Thus, grafting g-C₃N₄ with diverse delocalization groups by replacing the tri-*s*-triazine structures or triazine hexagons can induce the in-plane π -electron redistribution and the formation of the intrinsic polarization electric field to favor directional transfer of photo-induced charge carriers. The widely investigated grafting groups include aromatic motifs, carbon nitride allotropes, and C-chains.^{66–68} Xu *et al.*⁶⁹ constructed a D-A system by incorporating thiophene-2,5-dicarbaldehyde (TDA) into the g-C₃N₄ network, and found that the modified g-C₃N₄ displayed an obviously improved photocatalytic performance for bisphenol A degradation and H₂ evolution from water-splitting. The experimental and calculation results (Fig. 5) showed that the grafted TDA molecule could act as an electron acceptor to promote intermolecular charge transfer, and the incorporated aromatic ring from TDA enhanced the π -delocalization as well as the light response, which were responsible for the remarkable improvement of photocatalytic activity. Song *et al.*⁷⁰ designed an allotrope of g-C₃N₄, g-C₂N₃, where the aromatic azide pentagons were incorporated into the triazine hexagons. The theoretical simulations indicated that the positive and negative charge centers demonstrated significant dislocation, which resulted in the formation of the intrinsic polarization electric field to break the Coulomb interaction of electron–hole pairs. Consequently, the designed g-C₂N₃ exhibited a very high photocatalytic H₂ evolution rate of 14.9 mmol h⁻¹ g⁻¹ without any cocatalysts (AQE = 19.9% at 420 nm), which was even 2.6 times that of the g-C₃N₄ loaded

with Pt. Moreover, Li and Wang *et al.*⁷¹ reported a gas-solid grafting method to prepare an asymmetric structure of g-C₃N₄ with aromatized terminals. The research demonstrated that the aromatization of the terminals enhanced the asymmetry of π -electron distribution, thereby providing a driving force to achieve the efficient charge transport and separation and improving the photocatalytic activity by 15.4 fold. Recently, Zhang and Wang *et al.*⁷² developed the ionothermal method *via* a molten salt mixture to provide a mild liquid environment for polymerization, then obtained the well-organized and highly active carbon nitride. Based on this, they reported the copolymerization of 5-amino-tetrazole with nucleobases in salt melts, and synthesized the allotropes of g-C₃N₄, poly-heptazine-imide (PHI) based carbon nitrides.⁷³ The incorporation of nucleobases induced the formation of the D-A structure, which greatly promoted charge transfer and separation, thus, the PHI-based carbon nitrides showed higher H₂ evolution activity than the melon-based counterparts. Then they further combined the copolymerization and ionothermal method to polymerize urea with a thiophene derivative (2-aminothiophene-3-carbonitrile) and obtained the condensed allotrope of g-C₃N₄ with separated positive and negative charge centers, which displayed enhanced light absorption and charge separation efficiency. The optimal photocatalytic H₂ evolution activity was about 212.3 $\mu\text{mol h}^{-1}$ with an AQE of 12% at 420 nm, much higher than the pure urea-derived counterpart (81.8 $\mu\text{mol h}^{-1}$).⁷⁴

In addition to the modification of molecules or functional groups, the incorporation of metals into the cage structure among heptazine rings is also frequently applied to regulate the electronic structure of g-C₃N₄. Currently, the reported doping metals mainly include transition metals, alkali metals, alkaline earth metals, and rare earth metals.^{75–77} According to coordination and orbital theory, the lone electron pairs of sp²-hybridized N atoms at the cage site can couple with the unoccupied orbital of metals, which can induce the in-plane π -electron redistribution and promote charge directional transfer. For instance, Song *et al.*⁷⁸ incorporated Li ions into the cage sites of g-C₃N₄

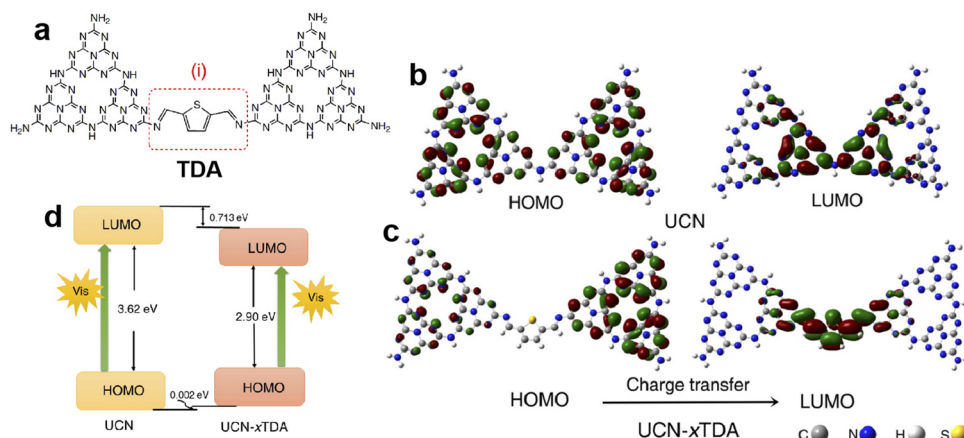


Fig. 5 The possible structure of TDA grafted g-C₃N₄ (a); the electronic structures of the HOMO and LUMO for (b) g-C₃N₄ derived from urea (UCN) and (c) TDA grafted g-C₃N₄ (UCN-xTDA); (d) the HOMO and LUMO levels for UCN and UCN-xTDA. Reproduced with permission from ref. 69. Copyright 2022, Royal Society of Chemistry.

to change the uniform π -electron distribution (Fig. 6a and b). The mülliken charge results showed that the electrons preferentially concentrated around Li and C atoms at the triangular cave, implying the formation of an in-plane coupling electric field, which favored charge directional transfer. As expected, the Li doped $\text{g-C}_3\text{N}_4$ exhibited a much lower charge recombination rate and higher H_2 evolution activity of $0.418 \text{ mmol h}^{-1}$ ($\sim 14000 \mu\text{mol h}^{-1} \text{ g}^{-1}$, AQE = 22.9% at 420 nm) compared with pristine $\text{g-C}_3\text{N}_4$ (0.009 mmol h^{-1}).

It is noted that the size of the triangular cave among the tri-s-triazine units of $\text{g-C}_3\text{N}_4$ is about 0.47 nm,⁷⁹ which is suitable for accommodating metals with smaller atomic diameters, such as Li and Na, *etc.* The large-sized alkali/alkaline earth metals, such as K, Rb, and Cs, would be incorporated into the interlayers of $\text{g-C}_3\text{N}_4$. Meanwhile, the transition metals with different shapes and directions of d orbitals can also be doped between layers instead of the triangular cave, due to the exclusion between the complex d orbitals and N 2p_z orbital at the cave site. Thus, the electronic interaction between the interlayer metals and the layers would induce the formation of an interlayer charge transport channel, which favors charge transfer among the layers of $\text{g-C}_3\text{N}_4$. Yang *et al.*⁸⁰ reported a series of In³⁺ doped $\text{g-C}_3\text{N}_4$ *via* a facile *in-situ* thermal copolymerization approach, and found that the In³⁺ ions were more easily doped into the interlayer of $\text{g-C}_3\text{N}_4$ due to the lower calculated energy of the out-of-plane configuration (Fig. 6c and d). The differential charge density result showed an obvious difference in electron density between doped In and $\text{g-C}_3\text{N}_4$, which facilitated the charge migration in $\text{g-C}_3\text{N}_4$. Therefore, the optimal In³⁺ doped $\text{g-C}_3\text{N}_4$ exhibited an excellent photocatalytic H_2 evolution activity of $1.35 \text{ mmol h}^{-1} \text{ g}^{-1}$, 17 fold that of pristine $\text{g-C}_3\text{N}_4$. Fu *et al.*⁸¹ incorporated $\text{g-C}_3\text{N}_4$ with single-atom Cu, which was bonded with compositional N in two ways, in-plane bonding and interlayer bonding. The characterization results demonstrated that

two groups of Cu-N_x as different charge transfer channels could promote the in-plane and interlayer charge transport, respectively, thereby greatly improving photocatalytic performance. Consequently, the Cu decorated $\text{g-C}_3\text{N}_4$ displayed a robust H_2 production rate of $10.6 \text{ mmol h}^{-1} \text{ g}^{-1}$ (AQE = 9.2% at 420 nm), which was about 30 times higher than that of bulk $\text{g-C}_3\text{N}_4$.

3. Heterojunction construction

With regard to structural modulation of $\text{g-C}_3\text{N}_4$, *e.g.* the morphology and doping engineering discussed above, a driving force based on the structural potential difference is introduced to fight against the Coulomb interaction rather than directly weakening the Coulomb field strength. In fact, it is also considered as an efficient strategy to promote the dissociation of excitons (electron–hole pairs) into free charge carriers through weakening the Coulomb effect. According to the Coulomb field equation, $F_c = kq_e q_h / r^2$, the Coulombic attraction of electron–hole pairs decreases with increasing the bandgap of semiconductor photocatalysts (*i.e.*, increase in r value).⁸² Meanwhile, the semiconductors with large bandgap usually possess higher CB and lower VB positions, which facilitate the redox reactions. Thus, the wide bandgap property of photocatalysts is desired for weakening the Coulomb field strength and enhancing the redox ability, thereby improving the photocatalytic efficiency. However, a wide bandgap also leads to a weakened light response, and reduces the generation of photo-induced charges. Therefore, it is incompatible for single-component photocatalysts to possess a weakened Coulomb effect, sufficient redox capability, and large light-harvesting range, noticeably which are expected to be achieved by designing heterojunction photocatalysts.

For heterojunction systems, they are typically composed of two semiconductor materials with different band structures, which can be categorized as a straddling gap heterojunction (type I), broken gap heterojunction (type III), and staggered gap heterojunction (type II and Z-scheme).^{83,84} In type I heterojunctions (Fig. 7a), the two semiconductors exhibit nested band alignment. The photo-induced electrons and holes on semiconductor A migrate to semiconductor B, resulting in charge accumulation on semiconductor B, which in turn triggers the high recombination of electron–hole pairs. For type III heterojunctions (Fig. 7b), a broken gap alignment is observed, and the photogenerated electrons and holes cannot migrate or transfer to any semiconductor, which also leads to a high charge recombination rate. As for type II heterojunctions (Fig. 7c), the staggered gap between two semiconductors facilitates the spatial separation of electron–hole pairs. As we see, semiconductor A possesses higher CB and VB levels, its photo-induced electrons can transfer to the CB of semiconductor B, while the holes on the VB transfer in the opposite direction. Thus, the transferred electrons and holes accumulate on semiconductor B and semiconductor A, respectively, which realizes the spatial separation of charges. However, in type II heterojunctions, the original electrons and holes would repel the transferred charge

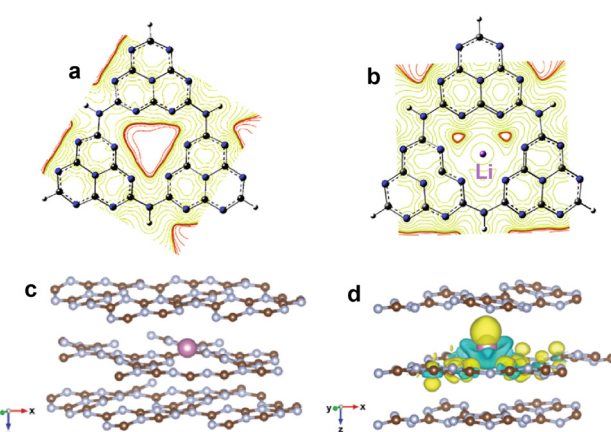


Fig. 6 Equipotential curve distribution on $\text{g-C}_3\text{N}_4$ (a) and Li doped $\text{g-C}_3\text{N}_4$ (b). Reproduced with permission from ref. 78. Copyright 2020, Elsevier. The optimized structure of $\text{g-C}_3\text{N}_4$ with interlayer In doping (c); differential charge density of In doped $\text{g-C}_3\text{N}_4$ (d), where the yellow and green isosurfaces represent the gain and loss of electrons, respectively. Reproduced with permission from ref. 80. Copyright 2021, Royal Society of Chemistry.

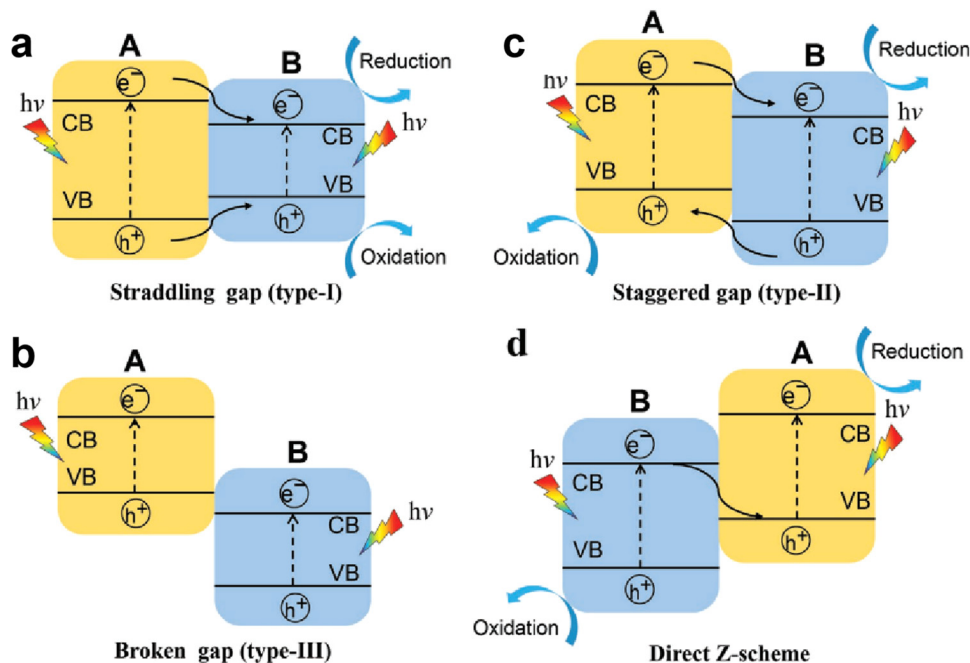


Fig. 7 Schematic illustration of the transfer paths of photo-induced charge carriers in different heterojunction systems: (a) straddling gap heterojunction (type I), (b) broken gap heterojunction (type III), and (c) and (d) staggered gap heterojunction (type II and Z-scheme). Reproduced with permission from ref. 83. Copyright 2020, Wiley-VCH.

carriers, and the work function difference of semiconductors also influences charge transfer, thus, a Z-scheme heterojunction with a band structure similar to type II heterojunctions is proposed as well (Fig. 7d). Typically, a built-in electric field (BIEF) is formed at the interface of semiconductors due to the work function difference, then the useless photogenerated electrons and holes recombine driven by the BIEF.⁸⁵ In this way, the remaining electrons and holes are left on semiconductor A and semiconductor B, respectively, achieving the effective separation of charge carriers and favorable redox capability for reaction. In this section, we focus on reviewing the charge separation and transfer processes in two heterojunction systems, Type II heterojunction and Z-scheme heterojunction. A comparison of the photocatalytic H₂ evolution activity of recent g-C₃N₄-based heterojunctions is given in Table 2.

3.1. Type II heterojunction

Among various g-C₃N₄ heterojunctions, type II g-C₃N₄ heterojunctions are the most common system. According to the charge transfer mechanism of the type II system,^{86,87} the CB and VB positions of g-C₃N₄ should be both higher or lower than those of another semiconductor in heterojunctions, thereby forming a staggered band structure that thermodynamically favors the subsequent charge transfer and realizes the spatial separation of electron–hole pairs. As a result, there are numerous studies about developing g-C₃N₄ heterojunctions with type II alignment to promote charge transfer during photocatalytic reaction, *e.g.*, CuFe₂O₄/g-C₃N₄,⁸⁸ ZnIn₂S₄/S-doped g-C₃N₄,⁸⁹ g-C₃N₄/r-TiO₂,⁹⁰ CsCu₂I₃/g-C₃N₄,⁹¹ β -AsP/g-C₃N₄,⁹² Cu₂O/g-C₃N₄,⁹³ B-doped C₃N₄/ZnO,⁹⁴ CoO_x/g-C₃N₄,⁹⁵ CeO₂/g-C₃N₄,⁹⁶ CdS/g-C₃N₄,⁹⁷ Zn_x

Cd_{1-x}In₂S₄/g-C₃N₄,⁹⁸ g-C₃N₄/SnS₂,⁹⁹ g-C₃N₄/Zn-MOF,¹⁰⁰ and CdSe/WS₂/g-C₃N₄,¹⁰¹ Ahmad *et al.*⁸⁸ developed a type II heterostructure of g-C₃N₄ combined with CuFe₂O₄, and found the CuFe₂O₄/g-C₃N₄ showed a 2.5-fold enhancement in photocatalytic activity and high AQE for H₂ evolution (25% at 450 nm). The obviously improved photocatalytic activity was mainly attributed to the thermodynamically optimal band alignment that facilitated directional charge transfer and obtained spatially separated electrons (on g-C₃N₄) and holes (on CuFe₂O₄) for efficient catalytic reaction. Xie and Luo *et al.*⁸⁹ utilized a simple *in-situ* hydrothermal method to construct S-doped g-C₃N₄ with ZnIn₂S₄ as a type II photocatalyst for splitting H₂O into H₂. Compared to single S-doped g-C₃N₄ and ZnIn₂S₄, the constructed heterojunction displayed a much higher photocatalytic H₂ production performance of 1.63 mmol h⁻¹ g⁻¹ (AQE = 0.90% at 420 nm), which was respectively an 8-fold and 3-fold enhancement in photocatalytic activity for S-doped g-C₃N₄ and ZnIn₂S₄. Additionally, Jiang *et al.*⁹⁵ reported a tunable heterojunction photocatalyst of cobalt oxide (CoO_x) confined in g-C₃N₄ nanotubes, where the type II heterojunction of CoO/g-C₃N₄ and type I heterojunction of Co₃O₄/g-C₃N₄ were obtained. The results showed that the prepared two heterojunctions of CoO_x/g-C₃N₄ both exhibited better photocatalytic performance than the CoO_x and g-C₃N₄. And the CoO/g-C₃N₄ with type II band alignment exhibited higher photocatalytic H₂ evolution activity than the Co₃O₄/g-C₃N₄ counterpart, which was mainly due to the longer lifetime of charge carriers, faster charge transfer, and higher charge separation efficiency in the type II heterojunction of CoO/g-C₃N₄. Recently, ternary heterojunctions with band coupling structures of type II/type II were designed to further accelerate the charge separation and transfer, and thus enhance

Table 2 Photocatalytic H_2 evolution activity of recent $g\text{-C}_3\text{N}_4$ -based heterojunctions

| Photocatalyst | Type | Light source | Reaction conditions | H_2 evolution rate | AQE | Ref. |
|--|--------------|-------------------------------------|--|---|------------------|------|
| $\text{CuFe}_2\text{O}_4/g\text{-C}_3\text{N}_4$ | Type II | 200 W Xe lamp | 20 mg catalyst, TEOA solution | 700.3 $\mu\text{mol h}^{-1} \text{g}^{-1}$ | 25% at 450 nm | 88 |
| $\text{ZnIn}_2\text{S}_4/g\text{-C}_3\text{N}_4$ | Type II | 300 W Xe lamp ($\lambda > 420$ nm) | 50 mg catalyst, TEOA solution, Pt cocatalyst | 1.63 $\mu\text{mol h}^{-1} \text{g}^{-1}$ | 0.90% at 420 nm | 89 |
| $\text{CoO}/g\text{-C}_3\text{N}_4$ | Type II | 300 W Xe lamp ($\lambda > 420$ nm) | 40 mg catalyst, TEOA ^a solution | 263 $\mu\text{mol h}^{-1} \text{g}^{-1}$ | 1.9% at 420 nm | 95 |
| $\text{CdSe/WS}_2/g\text{-C}_3\text{N}_4$ | Type II | White LED | 5 mg catalyst, TEOA solution | 1.29 $\mu\text{mol h}^{-1} \text{g}^{-1}$ | — | 101 |
| $\text{BaTiO}_3/\text{Au}/g\text{-C}_3\text{N}_4$ | Z-scheme | 300 W Xe lamp (AM 1.5G) | 20 mg catalyst, TEOA solution | 1769.3 $\mu\text{mol h}^{-1} \text{g}^{-1}$ | — | 107 |
| $g\text{-C}_3\text{N}_4/\text{W}_1\text{O}_4\text{g}$ | Z-scheme | 300 W Xe lamp ($\lambda > 400$ nm) | 50 mg catalyst, TEOA solution, Pt cocatalyst | 523.1 $\mu\text{mol h}^{-1} \text{g}^{-1}$ | 23.1% at 420 nm | 116 |
| $\text{CoSeO}_3/g\text{-C}_3\text{N}_4$ | Z-scheme | 300 W Xe lamp | 20 mg catalyst, TEOA solution | 1459.2 $\mu\text{mol h}^{-1} \text{g}^{-1}$ | 39.9% at 584 nm | 117 |
| $\text{ZnIn}_2\text{S}_4/g\text{-C}_3\text{N}_4$ | Z-scheme | 300 W Xe lamp ($\lambda > 400$ nm) | 2 mg catalyst, TEOA solution | 14.8 $\mu\text{mol g}^{-1} \text{h}^{-1}$ | 0.516% at 400 nm | 119 |
| $g\text{-C}_3\text{N}_4/\text{Co-MOF}$ | Z-scheme | 225 W Xe lamp | 5 mg catalyst, ascorbic acid solution, Pt cocatalyst | 33.17 $\mu\text{mol h}^{-1} \text{g}^{-1}$ | — | 120 |
| $\text{Ti}_3\text{C}_2/\text{TiO}_2/g\text{-C}_3\text{N}_4$ | S-scheme | 300 W Xe lamp ($\lambda > 420$ nm) | 50 mg catalyst, TEOA solution Ti_3C_2 cocatalyst | 5540 $\mu\text{mol h}^{-1} \text{g}^{-1}$ | 5.81% at 420 nm | 125 |
| $\text{CuInS}_2/g\text{-C}_3\text{N}_4$ | S-scheme | 350 W Xe lamp ($\lambda > 365$ nm) | 20 mg catalyst, TEOA solution | 1024 $\mu\text{mol h}^{-1} \text{g}^{-1}$ | — | 126 |
| $\text{MnO}_2/\text{Cd}_{0.8}\text{Si}_0.2/g\text{-C}_3\text{N}_4$ | S-scheme | 300 W Xe lamp ($\lambda > 420$ nm) | TEOA solution, Pt cocatalyst | 11.42 $\mu\text{mol h}^{-1} \text{g}^{-1}$ | — | 127 |
| CNN/BDCN^p | Homojunction | 300 W Xe lamp ($\lambda > 300$ nm) | 40 mg catalyst, pure water, Pt and Co(OH)_2 cocatalyst | 823.5 $\mu\text{mol h}^{-1} \text{g}^{-1}$ | 5.95% at 400 nm | 130 |
| $\text{S-C}_3\text{N}_4/\text{C}_3\text{N}_4$ | Homojunction | 300 W Xe lamp ($\lambda > 420$ nm) | 20 mg catalyst, TEOA solution, Pt cocatalyst | 5548.1 $\mu\text{mol h}^{-1} \text{g}^{-1}$ | 0.33% at 420 nm | 131 |
| CN-NAK^c (triazine-heptazine) | Homojunction | 50 W LED ($\lambda > 420$ nm) | 50 mg catalyst, TEOA solution, Pt cocatalyst | 11.7 $\mu\text{mol h}^{-1} \text{g}^{-1}$ | 60% at 420 nm | 132 |
| PHI/PTI^d | Homojunction | 300 W Xe lamp ($\lambda > 420$ nm) | 50 mg catalyst, TEOA solution, Pt cocatalyst | 6970 $\mu\text{mol h}^{-1} \text{g}^{-1}$ | 42% at 420 nm | 133 |
| $g\text{-C}_3\text{N}_4/\text{BST}^e$ | Homojunction | 225 W Xe lamp | 5 mg catalyst, TEOA solution, Pt cocatalyst | 12.47 $\mu\text{mol h}^{-1} \text{g}^{-1}$ | — | 134 |

^a Triethylamine. ^b Boron-doped and nitrogen-deficient $g\text{-C}_3\text{N}_4$ nanosheets. ^c Triazine-heptazine-based carbon nitride. ^d Poly(heptazine-triazine) imides. ^e BST: C-N compound broken by triazine units.

the photocatalytic efficiency. For instance, a ternary hybrid photocatalyst of $\text{CdSe/WS}_2/g\text{-C}_3\text{N}_4$ was prepared by Liang and Chen *et al.*¹⁰¹ According to the band structures of pristine CdSe , WS_2 , and $g\text{-C}_3\text{N}_4$, the type II/type II heterostructure was concluded to form at the interfaces of $\text{CdSe/WS}_2/g\text{-C}_3\text{N}_4$, which could not only expand the light absorption range but also greatly promote charge separation and restrain recombination. As a result, the designed ternary $\text{CdSe/WS}_2/g\text{-C}_3\text{N}_4$ photocatalyst displayed significantly enhanced photocatalytic performance, achieving the maximum H_2 evolution rate of 1.29 $\mu\text{mol h}^{-1} \text{g}^{-1}$, which was 1.7 and 1.3 times greater than binary $\text{WS}_2/g\text{-C}_3\text{N}_4$ and $\text{CdSe/g-C}_3\text{N}_4$, respectively.

As discussed above, the type II band alignment can indeed accelerate the migration and transfer of photogenerated charge carriers, and thus enhance the photocatalytic efficiency. However, as indicated in Fig. 7c, the spatial separation of charge carriers in type II heterojunctions is at the expense of their redox abilities when the electrons and holes are accumulated in more positive and negative energy levels, respectively, resulting in a weakened driving force for the following redox reaction.

3.2. Z-scheme heterojunction

Compared to type II heterojunctions, the Z-scheme heterojunction not only favors the spatial separation of charge carriers and inhibits charge recombination, but also retains a high catalytic activity with the photogenerated electrons and holes at higher chemical potentials of CB and VB, respectively.¹⁰² Typically, in a Z-scheme photocatalyst (Fig. 7d), the close contact of two semiconductors induces the recombination of ineffective charges at the interface, resulting in an enlarged distance for the active charge carriers, which effectively weakens the Coulombic attraction of electron-hole pairs and in turns achieves a high charge separation efficiency. Therefore, among different heterojunction photocatalysts, Z-scheme heterojunctions have received more attention and research due to their combined advantages of enhanced charge separation efficiency, weakened Coulomb field strength, and favorable redox ability.

The first generation of Z-scheme heterojunctions based on mimicking the natural photosynthesis process was proposed by Bard in 1979,¹⁰³ where the electron acceptor/donor ion pairs (A/D) were used as the redox mediators (Fig. 8a), *e.g.*, I^-/IO_3^- , $\text{Fe}^{2+}/\text{Fe}^{3+}$, and $\text{Co}(\text{bpy})_3^{2+}/\text{Co}(\text{bpy})_3^{3+}$.^{104,105} Although the introduction of the redox couples is beneficial for charge separation, it also brings several issues that the reversible redox couples would compete with the reactants for reaction and their application is limited to the liquid phase systems. In order to address the drawbacks of the conventional Z-scheme heterojunctions, an all-solid-state Z-scheme heterojunction was developed by Tada *et al.*,¹⁰⁶ where the redox ion pairs were substituted by solid electron mediators (Fig. 8b), such as noble metals, carbon nanotubes/nanofibers, graphene, and other conductive materials. Li *et al.*¹⁰⁷ constructed an all-solid-state Z-scheme photocatalyst by combining BaTiO_3 and $g\text{-C}_3\text{N}_4$ as the main catalytic components, using Au nanoparticles as the electron mediator. The prepared Z-scheme $\text{BaTiO}_3/\text{Au}/g\text{-C}_3\text{N}_4$ was able to show enhanced charge separation efficiency while retaining the sufficient redox capability for reaction. Compared

to $\text{g-C}_3\text{N}_4$, the $\text{BaTiO}_3/\text{Au}/\text{g-C}_3\text{N}_4$ exhibited higher photocatalytic activity toward H_2 production and RhB degradation, particularly, an 18-fold enhancement in H_2 evolution rate was achieved. Wang and Li *et al.*¹⁰⁸ also designed an all-solid-state ternary Z-scheme photocatalyst by coupling $\text{g-C}_3\text{N}_4$, carbon dots (CDs) and TiO_2 , where the CDs were adopted as an electron mediator. They found that the $\text{g-C}_3\text{N}_4/\text{CDs}/\text{TiO}_2$ exhibited a high H_2 evolution activity of $580 \mu\text{mol h}^{-1} \text{g}^{-1}$, and surpassed the binary $\text{g-C}_3\text{N}_4/\text{TiO}_2$ by 1.6 times, which was attributed to the effective spatial separation of charge carriers and their fast transfer assisted by the CDs mediator.

Obviously, as the second-generation Z-scheme heterojunctions, all-solid-state photocatalysts can effectively solve the problems of the ion pair-mediated Z-scheme photocatalytic system. However, the loading of solid electron mediators on the surface of semiconductors can trigger a shielding effect, reducing the light absorption and utilization, and the widely used noble metal mediators would also increase the costs and limit the wide application. Subsequently, a mediator-free Z-scheme heterojunction of ZnO/CdS was designed to further optimize the charge transfer process in photocatalytic reaction,¹⁰⁹ and then Yu's group proposed the third-generation Z-scheme heterojunction without any mediators (Fig. 8c), namely the direct Z-scheme heterojunction or S-scheme heterojunction.^{110,111} In a direct Z-scheme photocatalytic system, the shortcomings of the above two Z-scheme heterojunctions can be overcome, such as the light-shielding effect induced by solid mediators, high cost caused by the loading of mediators, and the backward reactions due to the presence of redox ion pairs.

We can see that the band structure of the direct Z-scheme heterojunction is similar to that of type II heterojunctions, whereas the migration and transfer paths of charge carriers are different (Fig. 7c and 8c). In direct Z-scheme heterojunction photocatalysts, the charge reorganization would occur at the interface of two closely contacted semiconductors due to their differences in work function or Fermi level, that is, electrons can autonomously move from one semiconductor with a lower work function to another with a higher work function, forming a built-in electric field (BIEF) at the interface.¹¹² Subsequently, under light irradiation, the BIEF drives the separation and transfer of photogenerated electrons and holes, resulting in the recombination of useless charge carriers and leaving the

active charge carriers at more favorable redox potentials.^{113,114} Therefore, the direct Z-scheme heterojunction with a spontaneously formed BIEF at the interface exhibits a high charge separation efficiency and redox capability, while avoiding the defects of the first and second generation Z-scheme heterojunction photocatalysts (*i.e.*, electron mediator-coupled systems).

Due to these advantages, the development of $\text{g-C}_3\text{N}_4$ -based direct Z-scheme heterojunctions has received more attention than those traditional Z-scheme systems. Lately, numerous direct Z-scheme heterojunctions of $\text{g-C}_3\text{N}_4$ -coupled composites with robust photocatalytic activities have been reported, such as $\text{g-C}_3\text{N}_4/\text{Bi}_4\text{NbO}_8\text{Cl}$,¹¹⁵ $\text{g-C}_3\text{N}_4/\text{W}_{18}\text{O}_{49}$,¹¹⁶ $\text{CoSeO}_3/\text{g-C}_3\text{N}_4$,¹¹⁷ $\text{Bi}_4\text{O}_5\text{Br}_2/\text{g-C}_3\text{N}_4$,¹¹⁸ $\text{ZnIn}_2\text{S}_4/\text{g-C}_3\text{N}_4$,¹¹⁹ $\text{g-C}_3\text{N}_4/\text{Co-MOF}$,¹²⁰ $\text{CoS}/\text{g-C}_3\text{N}_4$,¹²¹ $\text{LaCoO}_3/\text{g-C}_3\text{N}_4$,¹²² $\text{hBN}/\text{g-C}_3\text{N}_4$,¹²³ $\text{g-C}_3\text{N}_4/\text{Bi}_2\text{MoO}_6$,¹²⁴ $\text{Ti}_3\text{C}_2/\text{TiO}_2/\text{g-C}_3\text{N}_4$,¹²⁵ $\text{CuInS}_2/\text{g-C}_3\text{N}_4$,¹²⁶ and $\text{Mn}_{0.2}\text{Cd}_{0.8}\text{S}/\text{g-C}_3\text{N}_4$.¹²⁷ Typically, Zou *et al.*¹¹⁶ constructed a $\text{C}_3\text{N}_4/\text{W}_{18}\text{O}_{49}$ composite and found that the Fermi level of $\text{g-C}_3\text{N}_4$ could be uplifted through the adsorption of triethanolamine (TEOA), thereby transforming the composite from type II to direct Z-scheme (Fig. 9a and b). The $\text{C}_3\text{N}_4/\text{W}_{18}\text{O}_{49}$ composite with efficient Z-scheme charge transfer exhibited much higher photocatalytic activity compared with pure $\text{g-C}_3\text{N}_4$ and type-II $\text{C}_3\text{N}_4/\text{W}_{18}\text{O}_{49}$, resulting in a H_2 evolution rate of $5231 \mu\text{mol h}^{-1} \text{g}^{-1}$ and AQE of 23.1% at 420 nm (Fig. 9c). Dong and Cao *et al.*¹¹⁷ reported a novel CoSeO_3 assisted $\text{g-C}_3\text{N}_4$ composite with a Z-scheme structure. After combining with CoSeO_3 , the $\text{CoSeO}_3/\text{g-C}_3\text{N}_4$ displayed an expanded light absorption range, reduced charge transfer resistance and accelerated charge separation, and the optimal photocatalytic H_2 evolution activity of $\text{CoSeO}_3/\text{g-C}_3\text{N}_4$ was about 65 times that of pristine $\text{g-C}_3\text{N}_4$. Similarly, Dai and Zhang *et al.*¹²⁷ designed an S-scheme heterojunction photocatalyst of $\text{Mn}_{0.2}\text{Cd}_{0.8}\text{S}/\text{g-C}_3\text{N}_4$ through an *in-situ* hydrothermal growth process. The characterization results showed that the $\text{Mn}_{0.2}\text{Cd}_{0.8}\text{S}/\text{g-C}_3\text{N}_4$ hybrid possessed an intimate interface and favorable S-scheme band alignment, which could promote the charge transfer at the interface and increase the lifetime of reactive charge carriers, as well as retain the high redox capacity. The photocatalytic H_2 production activity of $\text{Mn}_{0.2}\text{Cd}_{0.8}\text{S}/\text{g-C}_3\text{N}_4$ reached $11.42 \text{ mmol h}^{-1} \text{g}^{-1}$, which was much higher than that of the original $\text{g-C}_3\text{N}_4$ and $\text{Mn}_{0.2}\text{Cd}_{0.8}\text{S}$.

Besides these, recently, the isotype heterojunctions of $\text{g-C}_3\text{N}_4$ -based composites have also been discussed and investigated due to their better lattice matching and compatibility,

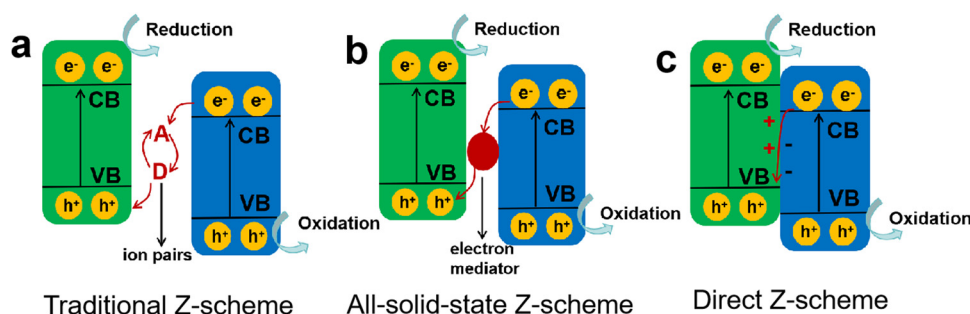


Fig. 8 Different types of Z-scheme heterojunctions: (a) traditional Z-scheme, (b) all-solid-state Z-scheme, (c) direct Z-scheme.

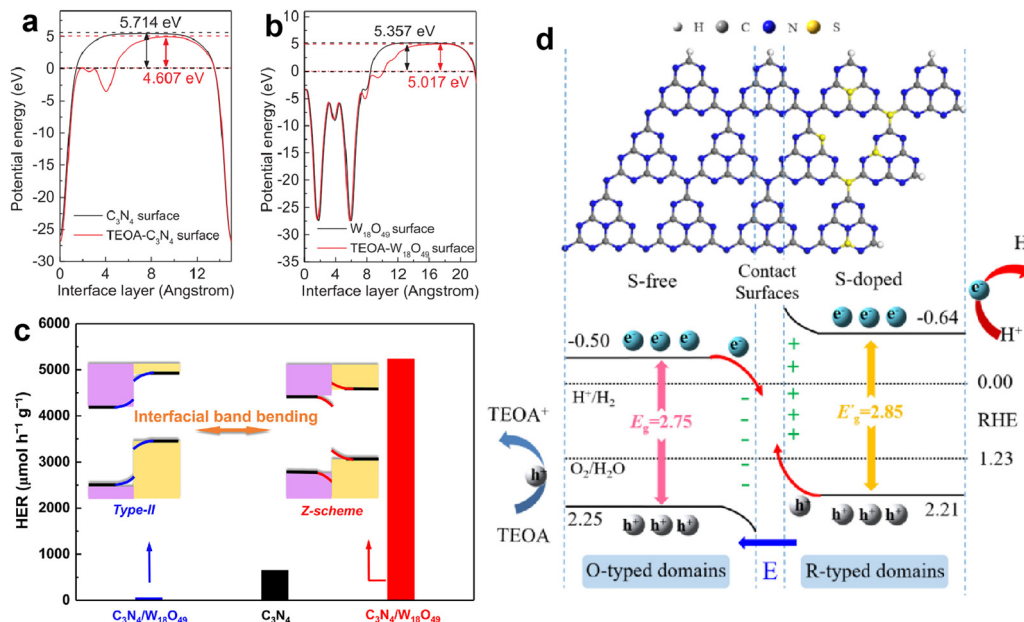


Fig. 9 The calculated work functions of $\text{g-C}_3\text{N}_4$ (a) and $\text{W}_{18}\text{O}_{49}$ (b) surfaces with and without TEOA; photocatalytic H_2 evolution activities of pure $\text{g-C}_3\text{N}_4$, type II $\text{g-C}_3\text{N}_4/\text{W}_{18}\text{O}_{49}$, and Z-scheme $\text{g-C}_3\text{N}_4/\text{W}_{18}\text{O}_{49}$ (c). Reproduced with permission from ref. 116. Copyright 2017, Elsevier. The structural configuration and charge transfer mechanism of S-doped $\text{g-C}_3\text{N}_4/\text{g-C}_3\text{N}_4$ isotype heterojunction (d). Reproduced with permission from ref. 131. Copyright 2022, Elsevier.

which are beneficial to the separation and transfer of photo-induced charge carriers at the interface.^{128–131} Shen *et al.*¹³⁰ prepared a series of $\text{g-C}_3\text{N}_4$ nanosheets with different contents of B dopants and N defects, resulting in the formation of $\text{g-C}_3\text{N}_4$ with controllable band structures, which could be applied as an O_2 -evolving component and combined with the original $\text{g-C}_3\text{N}_4$ as a H_2 -evolving component to construct an isotype Z-scheme heterojunction for overall water splitting. The obtained $\text{g-C}_3\text{N}_4$ self-based heterojunction displayed excellent photocatalytic activity, and the optimal H_2 and O_2 production rates achieved stoichiometric values of 32.94 and 16.42 $\mu\text{mol h}^{-1}$ (AQE of 5.95% at 400 nm). The superior photocatalytic performance was attributed to the strong interfacial interaction, favorable redox ability, and efficient charge transfer through the interfacial Z-scheme route. Jiang *et al.*¹³¹ also reported a novel isotype heterostructure of S-doped $\text{g-C}_3\text{N}_4/\text{g-C}_3\text{N}_4$ with S-scheme band alignment (Fig. 9d), which exhibited high photocatalytic H_2 evolution activity of 5548.1 $\mu\text{mol h}^{-1} \text{g}^{-1}$ (AQE of 0.43% at 420 nm) and remarkable durability for 24 h, nearly 49 times that of pure $\text{g-C}_3\text{N}_4$. Zhang and Wang *et al.*¹³² prepared a triazine-heptazine based copolymer with the internal donor-acceptor heterostructure, which greatly accelerated the interface charge transfer and achieved high photocatalytic H_2 evolution activity with an AQE of 60% at 420 nm. Afterwards, they also fabricated binary poly(heptazine-triazine) imides with semi-coherent interfaces. The fine lattice compatibility and intimate contact interface induced the formation of the built-in electric field, which facilitated rapid charge separation and transfer, resulting in a high AQE of 42% at 420 nm, even 64% by using K_2HPO_4 as the charge mediator.¹³³ Additionally, Shi *et al.*¹³⁴ also developed a $\text{g-C}_3\text{N}_4$ homojunction by decorating

the broken *s*-triazine unit C–N compound, which was tightly anchored on the $\text{g-C}_3\text{N}_4$ and could extract photogenerated electrons from $\text{g-C}_3\text{N}_4$. Furthermore, the broken *s*-triazine units provided active sites to grab H^+ , thereby promoting the H^+ reduction and achieving a fourfold improvement in H_2 evolution activity.

4. Cocatalyst loading

In addition to the heterojunction of coupling two semiconductors, loading metal-based cocatalysts on the surface of photocatalysts can also greatly promote the separation and transfer of photo-induced charge carriers, and then improve photocatalytic H_2 production activity, such as the reported Pt loaded $\text{g-C}_3\text{N}_4$, CdS and TiO_2 , and they all exhibited better photocatalytic performance than their original counterparts.^{135–137} The role of cocatalyst in improving photocatalytic activity is as follows:¹³⁸ on the one hand, the cocatalyst can serve as an electron trap to capture photogenerated electrons from the CB level of the semiconductor photocatalyst and retain the holes on the semiconductor, which achieve spatial separation of charge carriers and effectively suppress the recombination; on the other, the cocatalyst can provide abundant catalytic sites and reduce the activation energy of the H_2 evolution reaction. Fig. 10a shows a schematic diagram of the role of cocatalysts in photocatalytic water splitting. In order to achieve state-of-the-art photocatalytic activity, the cocatalysts should display suitable band alignment with the semiconductor, strong conductivity, and high catalytic activity toward H_2 evolution.^{139,140} According to the requirements of cocatalysts, H_2 -evolution electrocatalysts with excellent catalytic activity are commonly considered as promising

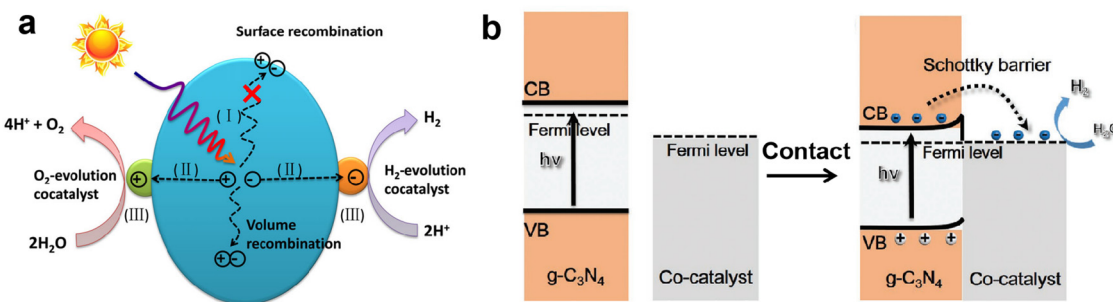


Fig. 10 The role of cocatalyst in photocatalytic water splitting (a). Reproduced with permission from ref. 139. Copyright 2020, Wiley-VCH. The band alignment between metallic cocatalysts and n-type $\text{g-C}_3\text{N}_4$ after intimate contact (b). Reproduced with permission from ref. 140. Copyright 2021, Wiley-VCH.

cocatalysts for photocatalytic H_2 production.^{141–143} Most electrocatalysts have lower Fermi levels (larger work functions), which is conducive to capturing photogenerated electrons, and their high catalytic activity can also boost the kinetics of surface H_2 evolution reaction. We previously prepared the VS_2 electrocatalyst with excellent catalytic activity toward H_2 evolution, and loaded it on $\text{g-C}_3\text{N}_4$ as a cocatalyst.^{27,144} Compared to pure $\text{g-C}_3\text{N}_4$, the VS_2 supported $\text{g-C}_3\text{N}_4$ displayed much higher photocatalytic H_2 evolution activity, a nearly 30 times increase. Our characterization and calculation results clearly revealed that the loading of VS_2 obviously improved the charge separation efficiency and reduced the energy barrier for H_2 evolution.

For the n-type $\text{g-C}_3\text{N}_4$ semiconductor, its Fermi level is close to the CB and generally higher than that of the metal-based cocatalysts, that is, the smaller work function of $\text{g-C}_3\text{N}_4$ ($\phi_{\text{g-C}_3\text{N}_4} < \phi_{\text{cocatalyst}}$). When the $\text{g-C}_3\text{N}_4$ surface is in intimate contact with the cocatalyst, the interfacial electrons transfer and lead to the formation of a Helmholtz double layer at the cocatalyst- $\text{g-C}_3\text{N}_4$ junction, where the $\text{g-C}_3\text{N}_4$ is positively charged and the cocatalyst is negatively charged. The established electric field between $\text{g-C}_3\text{N}_4$ and cocatalyst causes the band edges of $\text{g-C}_3\text{N}_4$ to bend upwards, forming an energy barrier called the Schottky barrier.^{145,146} Although the presence of a Schottky barrier at the interface would affect the charge transfer, the photogenerated electrons with sufficient energy can still flow from $\text{g-C}_3\text{N}_4$ to the cocatalyst through the Schottky barrier. Meanwhile, the rectification characteristic of the Schottky barrier suppresses the back recombination of charge carriers, ensuring the directional charge transfer and improving charge separation efficiency.^{147,148} Therefore, a perfect match of $\text{g-C}_3\text{N}_4$ and cocatalyst and the appropriate Schottky barrier are necessary to facilitate the interfacial charge transfer, prolong the lifetime of charge carriers, and improve photocatalytic H_2 production activity.

In this section, typical noble metal-based cocatalysts and transition metal-derived cocatalysts are discussed, with a focus on the role of cocatalysts in charge separation and transfer. A comparison of the photocatalytic H_2 evolution activity of recent $\text{g-C}_3\text{N}_4$ loaded with different cocatalyst is given in Table 3.

4.1. Noble metal-based cocatalysts

Noble metals such as Pt, Pd, Ru, Ir, Rh, and Au have often been utilized as the cocatalysts for photocatalytic H_2 production, due

to their strong metallicity, high work function for electron transfer, and robust catalytic activity for H_2 evolution.^{149–151} Among them, Pt can form an ideal Pt-H bond with appropriate strength and then significantly reduce the activation energy of H_2 evolution, so that Pt shows the highest H_2 evolution activity.¹⁵² Consequently, Pt is the most commonly used cocatalyst for improving photocatalytic H_2 production performance. Wang and Domen *et al.*¹⁵³ compared the photocatalytic H_2 production activities of $\text{g-C}_3\text{N}_4$ loaded with various noble metal cocatalysts, including Ru, Rh, Pd, Ir, Pt, and Au, and found the Pt loaded $\text{g-C}_3\text{N}_4$ exhibited the highest photocatalytic activity toward H_2 evolution. Moreover, nanoscale noble metals with a strong plasmonic effect, such as Au, Ag, and Pt, can improve the absorption of visible light and provide many high-energy hot electrons for reaction, thus further enhancing the photocatalytic performance.^{154,155} Wang *et al.*¹⁵⁴ deposited Au nanoparticles on the surface of $\text{g-C}_3\text{N}_4$ and obtained the obviously enhanced photocatalytic H_2 evolution activity. The characterization revealed that the loaded Au nanoparticles played a dual role in the photocatalytic reaction. On one hand, the Au nanoparticles could improve the charge separation efficiency through capturing electrons from $\text{g-C}_3\text{N}_4$; on the other hand, the Au plasma could provide additional hot electrons for H^+ reduction. Hence, the accelerated charge transfer and increased number of electrons contributed to the enhanced photocatalytic activity of Au/ $\text{g-C}_3\text{N}_4$. Yang and Wang *et al.*¹⁵⁶ also investigated the effect of different sizes and shapes of Au nanocrystals on the photocatalytic performance of $\text{g-C}_3\text{N}_4$. Among the prepared Au/ $\text{g-C}_3\text{N}_4$, the 18-nm-sized Au nanosphere loaded $\text{g-C}_3\text{N}_4$ showed an excellent photocatalytic H_2 production activity of $540 \mu\text{mol h}^{-1} \text{g}^{-1}$ (AQE = 1.2% at 380 nm), far exceeding the larger-sized Au nanosphere and Au nanorod loaded $\text{g-C}_3\text{N}_4$ system. The superior H_2 evolution activity was attributed to the optimized Au nanocrystals in promoting charge transfer and extending the light-harvesting range. Although noble metals can effectively promote proton reduction, they are also active sites for the backward reaction of H_2 and O_2 . Thus, a noble metal/metal oxide cocatalyst with a core-shell structure was proposed to suppress backward reaction.^{157,158} For example, Zhang and Wang *et al.*¹⁵⁹ decorated poly(triazine imide)-based carbon nitride with a Rh/ Cr_2O_3 core-shell cocatalyst for H_2 evolution, and CoO_x as the O_2

Table 3 Photocatalytic H₂ evolution activity of recent g-C₃N₄ loaded with different cocatalyst

| Photocatalyst | Cocatalyst | Light source | Reaction conditions | H ₂ evolution rate | AQE | Ref. |
|---|---|-------------------------------------|--|--|------------------|------|
| Au/g-C ₃ N ₄ | Au | 300 W Xe lamp ($\lambda > 420$ nm) | 20 mg catalyst, TEOA solution | 159.9 $\mu\text{mol h}^{-1} \text{g}^{-1}$ | — | 154 |
| Au/g-C ₃ N ₄ | Au nanospheres | 300 W Xe lamp ($\lambda > 420$ nm) | 20 mg catalyst, TEOA solution | 540 $\mu\text{mol h}^{-1} \text{g}^{-1}$ | 1.2% at 380 nm | 156 |
| Rh/Cr ₂ O ₃ -CoO _x /PTI ^a | Rh/Cr ₂ O ₃ -CoO _x | 300 W Xe lamp | 100 mg catalyst, pure water | 4500 $\mu\text{mol h}^{-1} \text{g}^{-1}$ | 20.2% at 365 nm | 159 |
| Pt-CoO _x /PTI | Pt-CoO _x | 300 W Xe lamp | 100 mg catalyst, pure water | 2730 $\mu\text{mol h}^{-1} \text{g}^{-1}$ | 12% at 365 nm | 160 |
| TiO ₂ @Pt/g-C ₃ N ₄ | TiO ₂ @Pt | 300 W Xe lamp | 100 mg catalyst, pure water | 7.63 $\mu\text{mol h}^{-1} \text{g}^{-1}$ | 0.11% at 365 nm | 161 |
| PtAu/g-C ₃ N ₄ | PtAu | 300 W Xe lamp | 50 mg catalyst, Na ₂ S/Na ₂ SO ₃ solution | 1009 $\mu\text{mol h}^{-1} \text{g}^{-1}$ | 0.45% at 420 nm | 164 |
| PtNi/g-C ₃ N ₄ | PtNi | 300 W Xe lamp ($\lambda > 420$ nm) | 25 mg catalyst, TEOA solution | 9528 $\mu\text{mol h}^{-1} \text{g}^{-1}$ | 10.6% at 370 nm | 165 |
| Ni/TiO ₂ /g-C ₃ N ₄ | Ni | 300 W Xe lamp ($\lambda > 420$ nm) | 50 mg catalyst, TEOA solution | 134 $\mu\text{mol h}^{-1} \text{g}^{-1}$ | 15% at 420 nm | 170 |
| NiMo/g-C ₃ N ₄ | NiMo | 300 W Xe lamp ($\lambda > 420$ nm) | 20 mg catalyst, TEOA solution | 1785 $\mu\text{mol h}^{-1} \text{g}^{-1}$ | ~0.25% at 365 nm | 172 |
| NiCu/g-C ₃ N ₄ | NiCu | 5 W LED | 10 mg catalyst, TEOA solution | 2088 $\mu\text{mol h}^{-1} \text{g}^{-1}$ | 6.83% at 475 nm | 173 |
| Mo ₂ C@g-C ₃ N ₄ | Mo ₂ C | 300 W Xe lamp ($\lambda > 420$ nm) | 80 mg catalyst, TEOA solution | 651 $\mu\text{mol h}^{-1} \text{g}^{-1}$ | 1.44% at 400 nm | 178 |
| WC@g-C ₃ N ₄ | WC | 300 W Xe lamp ($\lambda > 420$ nm) | 50 mg catalyst, TEOA solution | 146.1 $\mu\text{mol h}^{-1} \text{g}^{-1}$ | — | 180 |
| Ni ₂ PrGO/g-C ₃ N ₄ | Ni ₂ P | 300 W Xe lamp ($\lambda > 420$ nm) | 10 mg catalyst, TEOA solution | 2922 $\mu\text{mol h}^{-1} \text{g}^{-1}$ | 5.6% at 420 nm | 187 |
| Cu ₃ P@g-C ₃ N ₄ | Cu ₃ P | 300 W Xe lamp ($\lambda > 420$ nm) | 20 mg catalyst, TEOA solution | 343 $\mu\text{mol h}^{-1} \text{g}^{-1}$ | — | 188 |
| MoP@g-C ₃ N ₄ | MoP | 300 W Xe lamp | 10 mg catalyst, TEOA solution | 3868 $\mu\text{mol h}^{-1} \text{g}^{-1}$ | 21.6% at 405 nm | 189 |
| NiCoP@g-C ₃ N ₄ | NiCoP | 300 W Xe lamp | 20 mg catalyst, TEOA solution | 5162 $\mu\text{mol h}^{-1} \text{g}^{-1}$ | 18.5% at 400 nm | 190 |
| Cu-Ni(OH) ₂ /g-C ₃ N ₄ | Cu-Ni(OH) ₂ | 300 W Xe lamp (AM 1.5 G) | 20 mg catalyst, TEOA solution | 2037 $\mu\text{mol h}^{-1} \text{g}^{-1}$ | — | 194 |
| Pt/Ni(OH) ₂ /g-C ₃ N ₄ | Pt/Ni(OH) ₂ | 300 W Xe lamp ($\lambda > 400$ nm) | 10 mg catalyst, TEOA solution | 3005 $\mu\text{mol h}^{-1} \text{g}^{-1}$ | 11.2% at 420 nm | 196 |
| Pt/NVC/g-C ₃ N ₄ | Pt/NVC | 300 W Xe lamp ($\lambda > 400$ nm) | 50 mg catalyst, TEOA solution | 800 $\mu\text{mol h}^{-1} \text{g}^{-1}$ | 0.20% at 420 nm | 197 |

^a PTI: poly(triazine imide) based carbon nitride.

evolution cocatalyst. The presence of a Cr₂O₃ layer prevented the O₂ transfer but facilitated the proton penetration, thereby hindering the backward reaction over Rh and achieving an AQE of 20.2% at 365 nm for overall water splitting, which was much higher than the Pt and CoO_x modified one (AQE = 12%).¹⁶⁰ Su *et al.*¹⁶¹ modified Pt/C₃N₄ with a TiO₂ thin layer, which effectively prevented the reverse reaction and photocorrosion. Compared with naked Pt/C₃N₄, TiO₂@Pt/C₃N₄ exhibited 130% enhanced overall efficiency of water splitting (AQE = 0.11% at 365 nm). In addition to pure noble metals, noble metal-based bimetallic alloys have also been extensively studied as cocatalysts to improve photocatalytic performance.^{162,163} The advantages of bimetallic alloys are related to the synergistic effect of two metals in tuning the electronic structure, work function and catalytic activity, which lead to efficient charge transfer and photoreduction reaction. For example, Pradhan *et al.*¹⁶⁴ synthesized pure metals (Pt, Au) and PtAu alloy loaded g-C₃N₄, respectively, and investigated their photocatalytic H₂ production activities. The PtAu alloy modified g-C₃N₄ exhibited better photocatalytic activity than the monometallic counterparts. A similar phenomenon of the improved photocatalytic performance was also observed in PtNi alloy loaded g-C₃N₄.¹⁶⁵

Although the loading of noble metal-based cocatalysts can significantly boost the photocatalytic activity of H₂ production, the high cost and scarcity of noble metal materials limit their large-scale applications. Therefore, the development of low-cost, abundant, and highly active non-noble metal-based cocatalysts is highly desired for photocatalytic H₂ production. During the next part, various transition metal-based cocatalysts are discussed.

4.2. Transition metal-based cocatalysts

Currently, there are many studies on transition metals as cocatalysts for photocatalytic H₂ production, such as Ni, Cu, and Co, *etc.*^{166–168} Among various transition metals, Ni has been widely studied as a cocatalyst for g-C₃N₄ because its work function ($\phi = 5.4$ eV) is close to that of Pt ($\phi = 5.7$ eV) and its Fermi level is more positive than the CB of g-C₃N₄, which facilitate the capture of photogenerated electrons from g-C₃N₄.¹⁶⁹ In the meantime, the Fermi level of Ni is more negative than the reduction potential of H⁺/H₂, which promotes the transferred electrons to participate in the reduction reaction. Wu *et al.*¹⁷⁰ deposited the single-atom Ni on TiO₂/g-C₃N₄ as a cocatalyst, which could capture photogenerated electrons from g-C₃N₄ and accelerate the H⁺ reduction, resulting in higher H₂ production activity (AQE of 15% at 420 nm) than the TiO₂/g-C₃N₄ without Ni cocatalyst. Do *et al.*¹⁷¹ also reported the obviously improved photocatalytic H₂ evolution activity of g-C₃N₄ and S-doped g-C₃N₄ when Ni was applied as the cocatalyst. Besides individual transition metals, transition metal-based alloys have also received widespread attention as cocatalysts for photocatalytic reaction. For example, Zhang and Wang *et al.*¹⁷² showed the drastically enhanced photocatalytic performance of g-C₃N₄ with NiMo alloy as the cocatalyst. The optimal H₂ production rate of NiMo alloy modified g-C₃N₄ was found to be 1785 $\mu\text{mol h}^{-1} \text{g}^{-1}$ (AQE of ~0.25% at 365 nm),

which was even comparable to the Pt/g-C₃N₄ (2250 $\mu\text{mol h}^{-1} \text{g}^{-1}$). A similar enhancement in photocatalytic H₂ production performance was also observed in Ni-Cu bimetallic cocatalyst loaded g-C₃N₄, which exhibited excellent photocatalytic activity, about 24 and 2 times that of g-C₃N₄ and Ni/g-C₃N₄, respectively.¹⁷³ As mentioned above, the photocatalytic activity of g-C₃N₄ can be obviously improved by loading transition metals and their alloys. However, compared with the benchmark cocatalyst Pt, although most transition metals can effectively capture photogenerated electrons and improve charge separation efficiency, their catalytic activities toward H₂ evolution are lower than Pt, resulting in the lower photocatalytic performance of transition metal cocatalyst modified g-C₃N₄ than that of Pt loaded g-C₃N₄.

As we know, the intrinsic activity of catalysts is closely related to their electronic structures; exploring transition metal-derived cocatalysts with Pt-like electronic properties is necessary for further boosting photocatalytic H₂ evolution. Levy *et al.*¹⁷⁴ reported that carbonized tungsten (WC) exhibited Pt-like catalytic activity in hydrogenolysis and isomerization reactions. Subsequently, Bennett and coworkers carried out theoretical calculations to investigate the WC and found that the introduction of carbon into the tungsten changed its electronic distribution, resulting in the density of electronic states near the Fermi level close to Pt, which contributed to the Pt-like catalytic activity of WC.¹⁷⁵ Therefore, the transition metal-derived compounds as the substitute for Pt cocatalyst have received increasing attention in the field of photocatalytic H₂ production, including transition metal carbides, nitrides, phosphides, sulfides, *etc.*^{176–179} Li *et al.*¹⁸⁰ loaded the WC onto g-C₃N₄ and studied the effect of WC on photocatalytic H₂ production activity. It was demonstrated that the loaded WC as an efficient cocatalyst not only enhanced the surface H₂-evolution kinetics, but also served as an electron transfer channel to promote interfacial charge transfer. We previously studied the role of tungsten carbide (W₂C), tungsten sulfide (WS₂), and tungsten nitride (W₂N) in photocatalytic H₂ production and compared their catalytic activities.²⁸ We found that the W₂C loaded g-C₃N₄ exhibited the highest H₂ evolution activity. Based on the above study, we also designed a carbonized MoS₂ (MoS₂/Mo₂C) as the cocatalyst for g-C₃N₄, and demonstrated its superior photocatalytic activity to that of the pure MoS₂ loaded one, nearly 6 times higher in the rate of H₂ evolution.¹⁸¹ Thus, transition metal carbides as the alternative for noble metal Pt have prominent advantages and potential application value.

Similar to metal carbides, many metal phosphides display high electrocatalytic activity toward H₂ evolution, such as Ni₂P, CoP, MoP, Cu₃P, *etc.*¹⁸² And the use of metal phosphides as cocatalysts can effectively improve the surface H₂ evolution kinetics and charge separation efficiency, thus achieving efficient photocatalytic H₂ production activity.^{183–186} For example, Huang and coworkers compared the effect of different Ni-based compounds as cocatalysts on rGO/g-C₃N₄, and revealed that the Ni₂P loaded rGO/g-C₃N₄ displayed better photocatalytic H₂ evolution activity than the NiS, Ni₃C, and Ni₃N loaded system.¹⁸⁷ Among these photocatalysts, the suitable band alignment between the Ni₂P and rGO/g-C₃N₄ obviously promoted

electron transfer from g-C₃N₄ to Ni₂P *via* the rGO medium, then the H₂ was produced on the Ni₂P reaction site. This work clearly demonstrated the advantages of metal phosphide cocatalysts in suppressing charge recombination and accelerating H₂ evolution. Furthermore, Liu *et al.*¹⁸⁸ synthesized two types of copper phosphide loaded g-C₃N₄, Cu₃P/g-C₃N₄ and Cu₉₇P₃/g-C₃N₄. The loading of copper phosphide significantly boosted the separation and transfer of photogenerated charge carriers, leading to an improved photocatalytic activity of Cu₃P and Cu₉₇P₃ loaded g-C₃N₄. Shi *et al.*¹⁸⁹ deposited the MoP as a cocatalyst on g-C₃N₄, the close interface induced the bonding state of Mo-N, which promoted photogenerated electron transfer to MoP and greatly improved the charge separation efficiency. Meanwhile, the loading of MoP also reduced the energy barrier for H₂ production. The designed MoP/g-C₃N₄ displayed a H₂ evolution activity of 3868 $\mu\text{mol h}^{-1} \text{g}^{-1}$ with an AQE of 21.6% at 405 nm. Moreover, Liu and Fan *et al.*¹⁹⁰ also designed a bimetallic phosphide NiCoP as the cocatalyst for g-C₃N₄ to further improve the photocatalytic performance. It was demonstrated that the rate of photocatalytic H₂ evolution over NiCoP/g-C₃N₄ was obviously higher than that over Ni₂P/g-C₃N₄ and Co₂P/g-C₃N₄, even better than that over Pt anchored g-C₃N₄. The improved activity of g-C₃N₄ was attributed to the formation of an appropriate Schottky barrier at the interface of NiCoP/g-C₃N₄, which could promote the directional migration of photo-excited electrons to the NiCoP cocatalyst and inhibit the back recombination. Meanwhile, the synergistic effect of bimetallics in NiCoP could further reduce the activation energy of H₂ evolution, thus accelerating the H⁺ reduction.

Recently, on the basis of single-component cocatalysts, dual cocatalysts and composite cocatalysts have gradually been developed.^{191–193} In dual catalyst decorated g-C₃N₄, the spatially separated dual cocatalysts serve as the reduction site and oxidation site to trap the electrons and holes from g-C₃N₄, respectively, thus greatly minimizing charge recombination. For example, the use of Cu and Ni(OH)₂ as dual cocatalysts for g-C₃N₄ showed better photocatalytic activity with the H₂ evolution amount exceeding the sum of single Cu and Ni(OH)₂ counterparts.¹⁹⁴ The improvement in photocatalytic activity was mainly attributed to the coupling of Cu and Ni(OH)₂ cocatalysts, which could drive the transfer of photogenerated electrons and holes to Cu and Ni(OH)₂ respectively, achieving the spatial separation of charge carriers. A combination of Pt and MnO_x was also reported as the dual cocatalysts to promote the separation, transfer, and utilization of photo-induced electron-hole pairs in CdS/g-C₃N₄.¹⁹⁵ It is known that loading cocatalysts with good metallicity and matched Fermi level can indeed favor the directional transfer of charge carriers from g-C₃N₄ to cocatalysts. In the subsequent catalytic reaction, most cocatalysts can display high catalytic activity toward the reduction of H⁺ to H₂, but confront an obstacle regarding the large energy barrier for water dissociation, which is the first step in H₂ evolution reaction under neutral or alkaline conditions. Thus, the composite cocatalysts capable of promoting charge separation and improving reaction kinetics of proton reduction and water dissociation are developed. Zou and

coworkers designed Pt cluster decorated Ni(OH)_2 as a composite cocatalyst for $\text{g-C}_3\text{N}_4$, where the electron sink (Pt) and hole sink (Ni(OH)_2) were included in one cocatalyst.¹⁹⁶ It was found that the $\text{g-C}_3\text{N}_4$ with spatially separated Pt– Ni(OH)_2 cocatalyst exhibited a lower charge recombination rate than the composite counterpart, which was attributed to the effective spatial separation of electron–hole pairs. While in terms of the redox reaction, the close contact of Pt and Ni(OH)_2 in the composite cocatalyst could synergistically promote H_2O dissociation and H^+ reduction, which could not be achieved in the spatially separated Pt– Ni(OH)_2 system. As a result, the $\text{g-C}_3\text{N}_4$ with Pt– Ni(OH)_2 composite cocatalyst displayed higher photocatalytic activity than the Pt, Ni(OH)_2 , and spatially separated Pt– Ni(OH)_2 loaded $\text{g-C}_3\text{N}_4$. We also investigated a composite cocatalyst of Pt/N doped VC (Pt/NVC) and found an improvement in the photocatalytic H_2 production activity of Pt/NVC/ $\text{g-C}_3\text{N}_4$ compared to NVC/ $\text{g-C}_3\text{N}_4$ and Pt/ $\text{g-C}_3\text{N}_4$.¹⁹⁷ Therefore, the highly efficient cocatalysts are expected to achieve a high charge separation efficiency and robust catalytic activity simultaneously, and the multifunctional composite cocatalyst with strong synergistic effect is a promising cocatalyst for photocatalytic reactions.

5. Summary and outlook

5.1. Summary

The easy preparation, low cost, visible-light response, suitable band structure, and high stability of metal-free $\text{g-C}_3\text{N}_4$ make it one of the most promising photocatalysts for H_2 production from water reduction reactions. However, the inherent Coulomb interaction of photogenerated electron–hole pairs and the existence of an interlayer potential barrier in $\text{g-C}_3\text{N}_4$ induce the severe bulk recombination of charge carriers, thus greatly reducing the number of active electrons involved in the surface reduction reaction. To oppose the charge recombination and improve the charge separation efficiency, various approaches have been adopted to promote the separation and transfer of photoexcited charge carriers through weakening their Coulomb attraction.

In this perspective, we summarized several common and effective strategies for assisting charge separation in the bulk and surface of $\text{g-C}_3\text{N}_4$, including structural modulation, heterojunction construction, and cocatalyst loading. In terms of structural modulation, we discussed the effects of crystal structure, morphology and doping on charge separation and migration. The $\text{g-C}_3\text{N}_4$ prepared by traditional high-temperature calcination shows poor crystallinity and many defects, resulting in a high charge recombination rate. Hence, many strategies have been developed to promote the polymerization of precursors and synthesize the highly crystalline $\text{g-C}_3\text{N}_4$, such as salt-assisted methods, microwave synthesis, and two-step calcination. Meanwhile, for bulk $\text{g-C}_3\text{N}_4$, the electrostatic barrier between layers can hinder charge transfer to the surface active sites and induce severe bulk recombination. Thus, many works about morphological tuning of $\text{g-C}_3\text{N}_4$ have been carried out to change the

original structure of layer-by-layer stacking and facilitate the charge transfer across the interlayers. Designing ultrathin $\text{g-C}_3\text{N}_4$ nanosheets effectively enlarges the distance between layers, thereby breaking the constraint of interlayer electrostatic barrier and reducing the bulk recombination of photogenerated charge carriers. Otherwise, the tubular morphology of $\text{g-C}_3\text{N}_4$ also favors charge transfer and separation within the bulk phase. When the 2D $\text{g-C}_3\text{N}_4$ bends to form the hollow tubular structure, an apparent potential difference is formed between the inner and outer surfaces of tubular $\text{g-C}_3\text{N}_4$, which could drive the electron transfer from the inner to the outer surface and greatly improve the bulk charge separation efficiency. Besides the morphological tuning, the doping strategy has also been widely used to regulate the structure of $\text{g-C}_3\text{N}_4$, thus facilitating the charge migration and achieving a high charge separation efficiency. In particular, the incorporation of metals and delocalization groups would break the planar π -conjugated structure of $\text{g-C}_3\text{N}_4$ and induce the redistribution of in-plane delocalized charges, which result in the formation of an intrinsic polarization electric field to promote the in-plane charge transfer along the potential difference. Therefore, the appropriate structural modulation of bulk $\text{g-C}_3\text{N}_4$ via crystallinity regulation, morphology and doping engineering can obviously suppress the charge recombination within the bulk and surface and then improve the charge separation efficiency.

Additionally, the design of $\text{g-C}_3\text{N}_4$ -based composites, including semiconductor combination and cocatalyst loading, is another effective approach to improve surface charge separation efficiency by promoting charge migration and transfer at the interface of composites. Among various $\text{g-C}_3\text{N}_4$ composites, the Z-scheme heterojunction has attracted much attention due to its advantage of the directional charge transfer driven by a built-in electric field. In a Z-scheme $\text{g-C}_3\text{N}_4$ heterojunction, the intimate contact of two semiconductors with different work functions induces interfacial charge reorganization and the formation of a built-in electric field at the interface, which can drive the photogenerated charges across the interface and consume ineffective charges, thus achieving the spatial separation of charge carriers and significantly minimizing the surface recombination. Similarly, for the cocatalyst loaded $\text{g-C}_3\text{N}_4$ system, the difference in work function also causes the charge rearrangement at the interface and results in the formation of a Schottky barrier, which controls the flow of the photogenerated electrons to the cocatalyst and suppresses the back recombination of charge carriers.

5.2. Outlook

This progress can indeed improve the separation efficiency of photogenerated electron–hole pairs and achieve robust photocatalytic H_2 evolution activity. However, the solar-to-hydrogen conversion efficiency of the $\text{g-C}_3\text{N}_4$ system still struggles to meet the commercial level, due to the difficulty in synergistically regulating the separation and transfer of whole charge carriers, including bulk phase separation and surface separation. For the above discussed studies, the crystallinity regulation, doping engineering, heterojunction design, and cocatalyst loading can greatly promote the charge transfer within the plane or at the interface, which effectively suppress the surface

recombination of charge carriers. While the morphological tuning mainly favors the charges to transfer from the bulk to surface, its role in promoting the surface charge separation is not so prominent. Therefore, although the above modification approaches have achieved many positive results, there are still certain limitations in improving the photocatalytic performance of g-C₃N₄ based on a single strategy since each strategy has its own advantages and weaknesses. To facilitate the charge transfer and separation both in the bulk phase and surface and achieve an excellent whole charge separation efficiency, it is essential to combine multiple methods to synergistically modify the pristine g-C₃N₄.

Furthermore, there is another issue that is often overlooked in the charge transfer process, the randomness of charge transfer paths. Although the introduction of a potential difference or built-in electric field in g-C₃N₄ can induce directional transfer of charge carriers from one component to another, the charge movement and transfer paths are random, which can easily trigger charge recombination during the charge migration. Thus, constructing charge transport channels to achieve ordered charge migration is another key to further improving charge separation efficiency and photocatalytic activity.

In the meantime, the transfer mechanism of photogenerated charge carriers and photocatalytic mechanism still need detailed and in-depth understanding and research, which directly affect the structural design of the g-C₃N₄ system. For instance, the type II and direct Z-scheme heterojunction systems possess similar band structures; precisely probing interfacial charge transfer is crucial to distinguishing the heterojunction types. Hence, it is necessary to combine various characterization techniques to investigate the behavior of photogenerated charge carriers in photocatalytic reactions, including the surface photovoltage technique, transient photocurrent response, electrochemical impedance spectroscopy (EIS), photoluminescence (PL), X-ray photoelectron spectroscopy (XPS), *etc.* In particular, the advanced characterizations of time-resolved technology and in-operando technology need to be developed to explore the dynamics and specific migration pathways of photogenerated charge carriers.

In summary, continuous efforts are required to develop novel and robust g-C₃N₄ photocatalytic systems for practical application. There are some recommendations for the design of g-C₃N₄ photocatalysts: (1) combining the advantages of multiple methods to modify g-C₃N₄ and improve the overall charge separation efficiency, including bulk phase and surface separation; (2) constructing efficient in-plane and interlayer joint charge transport channels to achieve ordered migration of overall photogenerated charge carriers; (3) developing various and advanced characterizations to clearly reveal the charge transfer and separation mechanism, thereby constructing the desired g-C₃N₄ system.

Author contributions

Mengmeng Shao: investigation, writing – original draft. Yangfan Shao: data curation, writing – review & editing. Hui Pan: conceptualization.

Conflicts of interest

There are no conflicts to declare.

Acknowledgements

This work was supported by the National Natural Science Foundation of China (12204263) and the Guangdong Basic and Applied Basic Research Foundation (2022A1515010628).

References

- Q. Hassan, A. Z. Sameen, H. M. Salman, M. Jaszcuz and A. K. Al-Jiboori, *J. Energy Storage*, 2023, **72**, 108404.
- H. Ishaq, I. Dincer and C. Crawford, *Int. J. Hydrogen Energy*, 2022, **47**, 26238–26264.
- H. Nishiyama, T. Yamada, M. Nakabayashi, Y. Maehara, M. Yamaguchi, Y. Kuromiya, Y. Nagatsuma, H. Tokudome, S. Akiyama, T. Watanabe, R. Narushima, S. Okunaka, N. Shibata, T. Takata, T. Hisatomi and K. Domen, *Nature*, 2021, **598**, 304–307.
- Y. Zhao, C. Ding, J. Zhu, W. Qin, X. Tao, F. Fan, R. Li and C. Li, *Angew. Chem., Int. Ed.*, 2020, **59**, 9653–9658.
- P. Zhou, I. A. Navid, Y. Ma, Y. Xiao, P. Wang, Z. Ye, B. Zhou, K. Sun and Z. Mi, *Nature*, 2023, **613**, 66–70.
- A. Fujishima and K. Honda, *Nature*, 1972, **238**, 37–38.
- R. Shen, D. Ren, Y. Ding, Y. Guan, Y. H. Ng, P. Zhang and X. Li, *Sci. China Mater.*, 2020, **63**, 2153–2188.
- C. Xu, D. Li, X. Liu, R. Ma, N. Sakai, Y. Yang, S. Lin, J. Yang, H. Pan, J. Huang and T. Sasaki, *Chem. Eng. J.*, 2022, **430**, 132861.
- Z. Luo, X. Ye, S. Zhang, S. Xue, C. Yang, Y. Hou, W. Xing, R. Yu, J. Sun, Z. Yu and X. Wang, *Nat. Commun.*, 2022, **13**, 2230.
- B. Debnath, S. Dhingra and C. M. Nagaraja, *Sol. RRL*, 2021, **5**, 2100226.
- L. Chen, X. Yu, Z. Hua, Q. Liu, V. An, L. Feng, J. Guo, X. Zhang, J. Li and B. Liu, *ACS Appl. Energy Mater.*, 2023, **6**, 3769–3777.
- D. Wei, Y. Ding and Z. Li, *Int. J. Hydrogen Energy*, 2020, **45**, 17320–17328.
- B. Li, W. Wang, J. Zhao, Z. Wang, B. Su, Y. Hou, Z. Ding, W.-J. Ong and S. Wang, *J. Mater. Chem. A*, 2021, **9**, 10270–10276.
- J. Xu, C. Sun, Z. Wang, Y. Hou, Z. Ding and S. Wang, *Chem. – Eur. J.*, 2018, **24**, 18512–18517.
- S. Wang, Y. Wang, S. L. Zhang, S.-Q. Zang and X. W. Lou, *Adv. Mater.*, 2019, **31**, 1903404.
- Z. Xiong, Y. Hou, R. Yuan, Z. Ding, W.-J. Ong and S. Wang, *Acta Phys.-Chim. Sin.*, 2022, **38**, 2111021.
- Z. Wang, B. Su, J. Xu, Y. Hou and Z. Ding, *Int. J. Hydrogen Energy*, 2020, **45**, 4113–4121.
- S. San Martín, M. J. Rivero and I. Ortiz, *Catalysts*, 2020, **10**, 901.
- H. Pan, *Renewable Sustainable Energy Rev.*, 2016, **57**, 584–601.

20 Y. Yang, W. Niu, L. Dang, Y. Mao, J. Wu and K. Xu, *Front. Chem.*, 2022, **10**, 955065.

21 G. Z. S. Ling, V. B.-Y. Oh, C. Y. Haw, L.-L. Tan and W.-J. Ong, *Energy Mater. Adv.*, 2023, **4**, 0038.

22 D. Ma, Z. Zhang, Y. Zou, J. Chen and J.-W. Shi, *Coord. Chem. Rev.*, 2024, **500**, 215489.

23 X. Wang, K. Maeda, A. Thomas, K. Takanabe, G. Xin, J. M. Carlsson, K. Domen and M. Antonietti, *Nat. Mater.*, 2009, **8**, 76–80.

24 X. Chen, R. Shi, Q. Chen, Z. Zhang, W. Jiang, Y. Zhu and T. Zhang, *Nano Energy*, 2019, **59**, 644–650.

25 X. Dang, M. Xie, F. Dai, J. Guo, J. Liu and X. Lu, *Adv. Mater. Interfaces*, 2021, **8**, 2100151.

26 M. Shao, Y. Shao, J. Chai, Y. Qu, M. Yang, Z. Wang, M. Yang, W. F. Ip, C. T. Kwok, X. Shi, Z. Lu, S. Wang, X. Wang and H. Pan, *J. Mater. Chem. A*, 2017, **5**, 16748–16756.

27 M. Shao, Y. Shao, S. Ding, J. Wang, J. Xu, Y. Qu, X. Zhong, X. Chen, W. F. Ip, N. Wang, B. Xu, X. Shi, X. Wang and H. Pan, *Appl. Catal., B*, 2018, **237**, 295–301.

28 M. Shao, W. Chen, S. Ding, K. H. Lo, X. Zhong, L. Yao, W. F. Ip, B. Xu, X. Wang and H. Pan, *ChemSusChem*, 2019, **12**, 3355–3362.

29 M. Li, Y. Gong, Y. Wang and T. He, *Phys. Chem. Chem. Phys.*, 2022, **24**, 19659–19672.

30 Q. Yao, H. Li, J. Xue, S. Jiang, Q. Zhang and J. Bao, *Angew. Chem., Int. Ed.*, 2023, **62**, e202308140.

31 Y. Bao, S. Song, G. Yao and S. Jiang, *Sol. RRL*, 2021, **5**, 2100118.

32 M. Z. Rahman and C. B. Mullins, *Acc. Chem. Res.*, 2019, **52**, 248–257.

33 Y. Kang, Y. Yang, L.-C. Yin, X. Kang, L. Wang, G. Liu and H.-M. Cheng, *Adv. Mater.*, 2016, **28**, 6471–6477.

34 W. Cui, P. Chen, L. Chen, J. Li, Y. Zhou and F. Dong, *J. Phys.: Energy*, 2021, **3**, 032008.

35 X. Chu, C. I. Sathish, J.-H. Yang, X. Guan, X. Zhang, L. Qiao, K. Domen, S. Wang, A. Vinu and J. Yi, *Small*, 2023, **19**, 2302875.

36 G. Zhang, Y. Xu, J. Zhu, Y. Li, C. He, X. Ren, P. Zhang and H. Mi, *Appl. Catal., B*, 2023, **338**, 123049.

37 N. P. Dharmarajan, D. Vidyasagar, J.-H. Yang, S. N. Talapaneni, J. Lee, K. Ramadass, G. Singh, M. Fawaz, P. Kumar and A. Vinu, *Adv. Mater.*, 2024, **36**, 2306895.

38 J. Wang and S. Wang, *Coord. Chem. Rev.*, 2022, **453**, 214338.

39 B. Zhao, W. Zhong, F. Chen, P. Wang, C. Bie and H. Yu, *Chin. J. Catal.*, 2023, **52**, 127–143.

40 Y. Li, D. Zhang, J. Fan and Q. Xiang, *Chin. J. Catal.*, 2021, **42**, 627–636.

41 F. He, Y. Hu, H. Zhong, Z. Wang, S. Peng and Y. Li, *Chem. Commun.*, 2023, **59**, 10476–10487.

42 F. Lin, S. Zhou, G. Wang, J. Wang, T. Gao, Y. Su and C.-P. Wong, *Nano Energy*, 2022, **99**, 107432.

43 S. An, Y. Guo, X. He, P. Gao, G. Hou, J. Hou, C. Song and X. Guo, *Appl. Catal., B*, 2022, **310**, 121323.

44 H. Song, X. Liu, Y. Wang, L. Chen, J. Zhang, C. Zhao, F. He, P. Dong, B. Li, S. Wang, S. Wang and H. Sun, *J. Colloid Interface Sci.*, 2022, **607**, 1603–1612.

45 Q. Wang, G. Zhang, W. Xing, Z. Pan, D. Zheng, S. Wang, Y. Hou and X. Wang, *Angew. Chem., Int. Ed.*, 2023, **62**, e202307930.

46 A. Torres-Pinto, C. G. Silva, J. L. Faria and A. M. T. Silva, *Catal. Today*, 2023, **424**, 113868.

47 H. Jing, M. You, S. Yi, T. Li, H. Ji, Y. Wang, Z. Zhang, R. Zhang, D. Chen and H. Yang, *ChemSusChem*, 2020, **13**, 827–837.

48 L. Lin, Z. Lin, J. Zhang, X. Cai, W. Lin, Z. Yu and X. Wang, *Nat. Catal.*, 2020, **3**, 649–655.

49 S. Gao, X. Wang, C. Song, S. Zhou, F. Yang and Y. Kong, *Appl. Catal., B*, 2021, **295**, 120272.

50 L. Wang, Y. Hong, E. Liu, X. Duan, X. Lin and J. Shi, *Carbon*, 2020, **163**, 234–243.

51 Y.-J. Yuan, Z. Shen, S. Wu, Y. Su, L. Pei, Z. Ji, M. Ding, W. Bai, Y. Chen, Z.-T. Yu and Z. Zou, *Appl. Catal., B*, 2019, **246**, 120–128.

52 C. Wu, S. Xue, Z. Qin, M. Nazari, G. Yang, S. Yue, T. Tong, H. Ghasemi, F. C. R. Hernandez, S. Xue, D. Zhang, H. Wang, Z. M. Wang, S. Pu and J. Bao, *Appl. Catal., B*, 2021, **282**, 119557.

53 Z. Jiang, X. Zhang, H.-S. Chen, X. Hu and P. Yang, *Chem-CatChem*, 2019, **11**, 4558–4567.

54 W. Luo, X. Chen, Z. Wei, D. Liu, W. Yao and Y. Zhu, *Appl. Catal., B*, 2019, **255**, 117761.

55 H. Pan, Y.-W. Zhang, V. B. Shenoy and H. Gao, *ACS Catal.*, 2011, **1**, 99–104.

56 Y. Zeng, X. Liu, C. Liu, L. Wang, Y. Xia, S. Zhang, S. Luo and Y. Pei, *Appl. Catal., B*, 2018, **224**, 1–9.

57 X. Pan and X. Bao, *Acc. Chem. Res.*, 2011, **44**, 553–562.

58 X. Pan and X. Bao, *Chem. Commun.*, 2008, 6271–6281.

59 X. Blase, L. X. Benedict, E. L. Shirley and S. G. Louie, *Phys. Rev. Lett.*, 1994, **72**, 1878–1881.

60 Z. Jiang, C. Jia, B. Wang, P. Yang and G. Gao, *J. Alloys Compd.*, 2020, **826**, 154145.

61 G. Jiang, X. You, B. An, F. Liu, X. Duan, Y. Wang, C. Liu and C. Zhao, *Appl. Catal., B*, 2022, **305**, 121018.

62 Z. Lin, Y. Zhao, J. Luo, S. Jiang, C. Sun and S. Song, *Adv. Funct. Mater.*, 2020, **30**, 1908797.

63 C. Xu, X. Liu, D. Li, Z. Chen, J. Yang, J. Huang and H. Pan, *ACS Appl. Mater. Interfaces*, 2021, **13**, 20114–20124.

64 J. Xie, C. Wang, N. Chen, W. Chen, J. Xu, P. Bai, B. Liu, L. Zhang and H. Wang, *J. Mater. Chem. C*, 2021, **9**, 4378–4384.

65 H. Che, C. Li, P. Zhou, C. Liu, H. Dong and C. Li, *Appl. Surf. Sci.*, 2020, **505**, 144564.

66 C. Xu, H. Liu, D. Wang, D. Li, Y. Zhang, X. Liu, J. Huang, S. Wu, D. Fan, H. Liu and H. Pan, *Appl. Catal., B*, 2023, **334**, 122835.

67 H. Fang, J. Gao, J. Wang, J. Xu and L. Wang, *Sep. Purif. Technol.*, 2023, **314**, 123565.

68 N. Wang, L. Cheng, Y. Liao and Q. Xiang, *Small*, 2023, **19**, 2300109.

69 C. Xu, X. Liu, H. Liu, D. Li, Y. Yang, S. Lin, D. Fan and H. Pan, *J. Mater. Chem. A*, 2022, **10**, 21031–21043.

70 D. Tang, C. Shao, S. Jiang, C. Sun and S. Song, *ACS Nano*, 2021, **15**, 7208–7215.

71 W. Luo, Y. Li, J. Wang, J. Liu, N. Zhang, M. Zhao, J. Wu, W. Zhou and L. Wang, *Nano Energy*, 2021, **87**, 106168.

72 G. Zhang, G. Li, T. Heil, S. Zafeiratos, F. Lai, A. Savateev, M. Antonietti and X. Wang, *Angew. Chem., Int. Ed.*, 2019, **58**, 3433–3437.

73 G. Zhang, M. Liu, T. Heil, S. Zafeiratos, A. Savateev, M. Antonietti and X. Wang, *Angew. Chem., Int. Ed.*, 2019, **58**, 14950–14954.

74 M. Chang, Z. Pan, D. Zheng, S. Wang, G. Zhang, M. Anpo and X. Wang, *ChemSusChem*, 2023, **16**, e202202255.

75 S. Wu, Y. Yu, K. Qiao, J. Meng, N. Jiang and J. Wang, *J. Photochem. Photobiol. A*, 2021, **406**, 112999.

76 J. Shen, C. Luo, S. Qiao, Y. Chen, Y. Tang, J. Xu, K. Fu, D. Yuan, H. Tang, H. Zhang and C. Liu, *ACS Catal.*, 2023, **13**, 6280–6288.

77 S. Tasleem and M. Tahir, *Int. J. Hydrogen Energy*, 2021, **46**, 20995–21012.

78 J. Luo, J. He, S. Jiang, C. Sun and S. Song, *Chem. Eng. J.*, 2020, **396**, 125365.

79 M. Zhou, G. Dong, F. Yu and Y. Huang, *Appl. Catal., B*, 2019, **256**, 117825.

80 X. Yang, Z. Guo, X. Zhang, Y. Han, Z. Xue, T. Xie and W. Yang, *New J. Chem.*, 2021, **45**, 544–550.

81 X. Xiao, Y. Gao, L. Zhang, J. Zhang, Q. Zhang, Q. Li, H. Bao, J. Zhou, S. Miao, N. Chen, J. Wang, B. Jiang, C. Tian and H. Fu, *Adv. Mater.*, 2020, **32**, 2003082.

82 J. He, Y. Zhao, S. Jiang and S. Song, *Sol. RRL*, 2021, **5**, 2000446.

83 Q. Su, Y. Li, R. Hu, F. Song, S. Liu, C. Guo, S. Zhu, W. Liu and J. Pan, *Adv. Sustainable Syst.*, 2020, **4**, 2000130.

84 X. Xu, X. Feng, W. Wang, K. Song, D. Ma, Y. Zhou and J.-W. Shi, *J. Colloid Interface Sci.*, 2023, **651**, 669–677.

85 H. Dong, L. Tong, P. Zhang, D. Zhu, J. Jiang and C. Li, *J. Mater. Sci. Technol.*, 2024, **179**, 251–261.

86 X. Kuang, X. Deng, Y. Ma, J. Zeng, B. Zi, Y. Zhang, J. Zhang, B. Xiao and Q. Liu, *J. Mater. Chem. C*, 2022, **10**, 6341–6347.

87 S. Yu, C. Li, Y. Lin, J. Zhang, Y. Liu and F. Yu, *Sep. Purif. Technol.*, 2024, **341**, 126888.

88 A. Mehtab, S. Banerjee, Y. Mao and T. Ahmad, *ACS Appl. Mater. Interfaces*, 2022, **14**, 44317–44329.

89 Y. Wang, J. Li, S. Chen, Y. Xie, Y. Ma, Y. Luo, J. Huang, Y. Ling, J. Ye, Y. Liang and J. Du, *J. Alloys Compd.*, 2022, **924**, 166569.

90 S. Wei, F. Wang, P. Yan, M. Dan, W. Cen, S. Yu and Y. Zhou, *J. Catal.*, 2019, **377**, 122–132.

91 Y. Lv, D. Ma, C. Yang, K. Song, L. Shi, Y. Cheng, C. Niu and J.-W. Shi, *Sep. Purif. Technol.*, 2023, **316**, 123813.

92 H. Zhao, B. Jia, Z. Wang, L. Han, H. Song and P. Lu, *Int. J. Hydrogen Energy*, 2023, **48**, 10051–10061.

93 A. Mehtab, Y. Mao, S. M. Alshehri and T. Ahmad, *J. Colloid Interface Sci.*, 2023, **652**, 1467–1480.

94 D. Kim and K. Yong, *Appl. Catal., B*, 2021, **282**, 119538.

95 Y. Zhu, T. Wan, X. Wen, D. Chu and Y. Jiang, *Appl. Catal., B*, 2019, **244**, 814–822.

96 X. Zhang, H. Liang, C. Li and J. Bai, *Inorg. Chem. Commun.*, 2022, **144**, 109838.

97 N. Güy, *Appl. Surf. Sci.*, 2020, **522**, 146442.

98 Y. Zou, J.-W. Shi, L. Sun, D. Ma, S. Mao, Y. Lv and Y. Cheng, *Chem. Eng. J.*, 2019, **378**, 122192.

99 Y. Liu, C. Lv, J. Sun, X. Zhou, Y. Zhou and G. Chen, *Adv. Mater. Interfaces*, 2022, **9**, 2200153.

100 D. Ma, J.-W. Shi, Z. Pu, S. Mao, X. Xu, D. He, R. Guo and F. Chen, *Sol. RRL*, 2022, **6**, 2200714.

101 J. Pan, J. Liang, Z. Xu, X. Yao, J. Qiu, H. Chen, L. Qin, D. Chen and Y. Huang, *Int. J. Hydrogen Energy*, 2021, **46**, 30344–30354.

102 J. Jia, Q. Zhang, K. Li, Y. Zhang, E. Liu and X. Li, *Int. J. Hydrogen Energy*, 2023, **48**, 196–231.

103 A. J. Bard, *J. Photochem.*, 1979, **10**, 59–75.

104 B.-J. Ng, L. K. Putri, X. Y. Kong, Y. W. Teh, P. Pasbakhsh and S.-P. Chai, *Adv. Sci.*, 2020, **7**, 1903171.

105 Y. Kang, H. Qi, G. Wan, C. Zhen, X. Xu, L.-C. Yin, L. Wang, G. Liu and H.-M. Cheng, *Joule*, 2022, **6**, 1876–1886.

106 H. Tada, T. Mitsui, T. Kiyonaga, T. Akita and K. Tanaka, *Nat. Mater.*, 2006, **5**, 782–786.

107 M. Wu, T. Ding, Y. Wang, W. Zhao, H. Xian, Y. Tian, T. Zhang and X. Li, *Catal. Today*, 2020, **355**, 311–318.

108 Z. Hu, D. Shi, G. Wang, T. Gao, J. Wang, L. Lu and J. Li, *Appl. Surf. Sci.*, 2022, **601**, 154167.

109 X. Wang, G. Liu, Z.-G. Chen, F. Li, L. Wang, G. Q. Lu and H.-M. Cheng, *Chem. Commun.*, 2009, 3452–3454.

110 J. Yu, S. Wang, J. Low and W. Xiao, *Phys. Chem. Chem. Phys.*, 2013, **15**, 16883–16890.

111 J. Fu, Q. Xu, J. Low, C. Jiang and J. Yu, *Appl. Catal., B*, 2019, **243**, 556–565.

112 Y. Lei, J. Ye, J. García-Antón and H. Liu, *Chin. J. Catal.*, 2023, **53**, 72–101.

113 H. Chen, S. Gao, G. Huang, Q. Chen, Y. Gao and J. Bi, *Appl. Catal., B*, 2024, **343**, 123545.

114 Q. Tang, W. Tao, J. Hu, T. Gui, Z. Wang, Y. Xiao, R. Song, Y. Jiang and S. Guo, *ACS Appl. Nano Mater.*, 2023, **6**, 17130–17139.

115 Y. You, S. Wang, K. Xiao, T. Ma, Y. Zhang and H. Huang, *ACS Sustainable Chem. Eng.*, 2018, **6**, 16219–16227.

116 Z.-F. Huang, J. Song, X. Wang, L. Pan, K. Li, X. Zhang, L. Wang and J.-J. Zou, *Nano Energy*, 2017, **40**, 308–316.

117 T. Feng, J. Jin, Y. Cao, H. Li, B. Dong and L. Cao, *Int. J. Hydrogen Energy*, 2022, **47**, 5999–6010.

118 X. Zhao, Y. You, S. Huang, Y. Wu, Y. Ma, G. Zhang and Z. Zhang, *Appl. Catal., B*, 2020, **278**, 119251.

119 M. Tan, Y. Ma, C. Yu, Q. Luan, J. Li, C. Liu, W. Dong, Y. Su, L. Qiao, L. Gao, Q. Lu and Y. Bai, *Adv. Funct. Mater.*, 2022, **32**, 2111740.

120 Z. Pu, B. Xiao, S. Mao, Y. Sun, D. Ma, H. Wang, J. Zhou, Y. Cheng and J.-W. Shi, *J. Colloid Interface Sci.*, 2022, **628**, 477–487.

121 Z.-x Bi, R.-t Guo, X.-y Ji, X. Hu, J. Wang, X. Chen and W.-g Pan, *Int. J. Hydrogen Energy*, 2022, **47**, 34430–34443.

122 R. Wang, C. Ye, H. Wang and F. Jiang, *ACS Omega*, 2020, **5**, 30373–30382.

123 L. Xu, J. Zeng, Q. Li, L. Xia, X. Luo, Z. Ma, B. Peng, S. X. Xiong, Z. Li, L.-L. Wang and Y. Lei, *Appl. Surf. Sci.*, 2021, **547**, 149207.

124 Y. Zhen, C. Yang, H. Shen, W. Xue, C. Gu, J. Feng, Y. Zhang, F. Fu and Y. Liang, *Phys. Chem. Chem. Phys.*, 2020, **22**, 26278–26288.

125 G. Dong, Y. Zhang, Y. Wang, Q. Deng, C. Qin, Y. Hu, Y. Zhou and G. Tian, *ACS Appl. Energy Mater.*, 2021, **4**, 14342–14351.

126 J. Zhang, Y. Zhao, K. Qi and S.-Y. Liu, *J. Mater. Sci. Technol.*, 2024, **172**, 145–155.

127 Z. Zhao, K. Dai, J. Zhang and G. Dawson, *Adv. Sustainable Syst.*, 2023, **7**, 2100498.

128 H. Sun, Y. Shi, W. Shi and F. Guo, *Appl. Surf. Sci.*, 2022, **593**, 153281.

129 Q. Xu, D. Ma, S. Yang, Z. Tian, B. Cheng and J. Fan, *Appl. Surf. Sci.*, 2019, **495**, 143555.

130 D. Zhao, Y. Wang, C.-L. Dong, Y.-C. Huang, J. Chen, F. Xue, S. Shen and L. Guo, *Nat. Energy*, 2021, **6**, 388–397.

131 J. Jiang, Z. Xiong, H. Wang, G. Liao, S. Bai, J. Zou, P. Wu, P. Zhang and X. Li, *J. Mater. Sci. Technol.*, 2022, **118**, 15–24.

132 G. Zhang, L. Lin, G. Li, Y. Zhang, A. Savateev, S. Zafeiratos, X. Wang and M. Antonietti, *Angew. Chem., Int. Ed.*, 2018, **57**, 9372–9376.

133 J. Zhang, X. Liang, C. Zhang, L. Lin, W. Xing, Z. Yu, G. Zhang and X. Wang, *Angew. Chem., Int. Ed.*, 2022, **61**, e202210849.

134 Y. Lv, D. Ma, K. Song, S. Mao, Z. Liu, D. He, X. Zhao, T. Yao and J.-W. Shi, *J. Mater. Chem. A*, 2023, **11**, 800–808.

135 Y. Hu, Y. Qu, Y. Zhou, Z. Wang, H. Wang, B. Yang, Z. Yu and Y. Wu, *Chem. Eng. J.*, 2021, **412**, 128749.

136 R. Feng, K. Wan, X. Sui, N. Zhao, H. Li, W. Lei, J. Yu, X. Liu, X. Shi, M. Zhai, G. Liu, H. Wang, L. Zheng and M. Liu, *Nano Today*, 2021, **37**, 101080.

137 S. Qin, N. Denisov, J. Will, J. Kolařík, E. Spiecker and P. Schmuki, *Sol. RRL*, 2022, **6**, 2101026.

138 L. Tian, X. Guan, S. Zong, A. Dai and J. Qu, *Catalysts*, 2023, **13**, 355.

139 X. Liu and H. Zhuang, *Int. J. Energy Res.*, 2021, **45**, 1480–1495.

140 Q. Zhu, Z. Xu, B. Qiu, M. Xing and J. Zhang, *Small*, 2021, **17**, 2101070.

141 R. Tong, Z. Sun, X. Wang, L. Yang, J. Zhai, S. Wang and H. Pan, *Int. J. Hydrogen Energy*, 2020, **45**, 18912–18921.

142 M. Saruyama, C. M. Pelicano and T. Teranishi, *Chem. Sci.*, 2022, **13**, 2824–2840.

143 R. Tong, K. W. Ng, X. Wang, S. Wang, X. Wang and H. Pan, *J. Mater. Chem. A*, 2020, **8**, 23202–23230.

144 Y. Qu, M. Shao, Y. Shao, M. Yang, J. Xu, C. T. Kwok, X. Shi, Z. Lu and H. Pan, *J. Mater. Chem. A*, 2017, **5**, 15080–15086.

145 S. A. Rawool, M. R. Pai, A. M. Banerjee, S. Nath, R. D. Bapat, R. K. Sharma, Jagannath, B. Dutta, P. A. Hassan and A. K. Tripathi, *ACS Appl. Mater. Interfaces*, 2023, **15**, 39926–39945.

146 Z. Zhuang, Y. Li, Z. Li, F. Lv, Z. Lang, K. Zhao, L. Zhou, L. Moskaleva, S. Guo and L. Mai, *Angew. Chem., Int. Ed.*, 2018, **57**, 496–500.

147 G. Z. S. Ling, S.-F. Ng and W.-J. Ong, *Adv. Funct. Mater.*, 2022, **32**, 2111875.

148 Q. Wang, Q. Liu, Y.-Y. Ma, H.-X. Bi, J. Du and Z.-G. Han, *Inorg. Chem. Front.*, 2024, **11**, 1238–1251.

149 T. Tong, B. Zhu, C. Jiang, B. Cheng and J. Yu, *Appl. Surf. Sci.*, 2018, **433**, 1175–1183.

150 Q. Yang, T. Wang, Z. Zheng, B. Xing, C. Li and B. Li, *Appl. Catal., B*, 2022, **315**, 121575.

151 Z. Yu, Y. Li, A. Torres-Pinto, A. P. LaGrow, V. M. Diaconescu, L. Simonelli, M. J. Sampaio, O. Bondarchuk, I. Amorim, A. Araujo, A. M. T. Silva, C. G. Silva, J. L. Faria and L. Liu, *Appl. Catal., B*, 2022, **310**, 121318.

152 S. Trasatti, *J. Electroanal. Chem. Interfacial Electrochem.*, 1972, **39**, 163–184.

153 K. Maeda, X. Wang, Y. Nishihara, D. Lu, M. Antonietti and K. Domen, *J. Phys. Chem. C*, 2009, **113**, 4940–4947.

154 Z. Guo, F. Dai, H. Yin, M. Zhang, J. Xing and L. Wang, *Colloid Interface Sci. Commun.*, 2022, **48**, 100615.

155 X. Li, H. Jiang, C. Ma, Z. Zhu, X. Song, H. Wang, P. Huo and X. Li, *Appl. Catal., B*, 2021, **283**, 119638.

156 Y. Guo, H. Jia, J. Yang, H. Yin, Z. Yang, J. Wang and B. Yang, *Phys. Chem. Chem. Phys.*, 2018, **20**, 22296–22307.

157 Z. Li, R. Li, H. Jing, J. Xiao, H. Xie, F. Hong, N. Ta, X. Zhang, J. Zhu and C. Li, *Nat. Catal.*, 2023, **6**, 80–88.

158 T. Takata, J. Jiang, Y. Sakata, M. Nakabayashi, N. Shibata, V. Nandal, K. Seki, T. Hisatomi and K. Domen, *Nature*, 2020, **581**, 411–414.

159 M. Liu, G. Zhang, X. Liang, Z. Pan, D. Zheng, S. Wang, Z. Yu, Y. Hou and X. Wang, *Angew. Chem., Int. Ed.*, 2023, **62**, e202304694.

160 M. Liu, C. Wei, H. Zhuzhang, J. Zhou, Z. Pan, W. Lin, Z. Yu, G. Zhang and X. Wang, *Angew. Chem., Int. Ed.*, 2022, **61**, e202113389.

161 Z. Han, X. Ning, Z. Yin, W. Zhen, G. Lu and B. Su, *Int. J. Hydrogen Energy*, 2024, **59**, 856–865.

162 Y. Liu, Z. Sun and Y. H. Hu, *Chem. Eng. J.*, 2021, **409**, 128250.

163 C. M. Pelicano, M. Saruyama, R. Takahata, R. Sato, Y. Kitahama, H. Matsuzaki, T. Yamada, T. Hisatomi, K. Domen and T. Teranishi, *Adv. Funct. Mater.*, 2022, **32**, 2202987.

164 K. Bhunia, M. Chandra, S. Khilari and D. Pradhan, *ACS Appl. Mater. Interfaces*, 2019, **11**, 478–488.

165 R. Li, Y. Wang, C. Zuo, J. Wang, X. Sheng, Y. Huang, Y. Zhang and Y. Zhou, *Int. J. Hydrogen Energy*, 2023, **48**, 28277–28288.

166 D. Ma, X. Zhang, C. Yang, X. Feng, Z.-F. Zhang, K. Song, S. Wu, L. Li, T. Jiang and J.-W. Shi, *Sep. Purif. Technol.*, 2023, **327**, 124996.

167 C. Wang, J. Xie, N. Chen, W. Chen, P. Bai and H. Wang, *ACS Appl. Energy Mater.*, 2021, **4**, 13796–13802.

168 T. Song, X. Zhang, K. Matras-Postolek and P. Yang, *J. Environ. Chem. Eng.*, 2022, **10**, 108747.

169 L. Ji, C. Lv, Z. Chen, Z. Huang and C. Zhang, *Adv. Mater.*, 2018, **30**, 1705653.

170 S. Yang, K. Wang, Q. Chen and Y. Wu, *J. Mater. Sci. Technol.*, 2024, **175**, 104–114.

171 M.-H. Vu, M. Sakar, C.-C. Nguyen and T.-O. Do, *ACS Sustainable Chem. Eng.*, 2018, **6**, 4194–4203.

172 X. Han, D. Xu, L. An, C. Hou, Y. Li, Q. Zhang and H. Wang, *Appl. Catal., B*, 2019, **243**, 136–144.

173 Z. Jin and L. Zhang, *J. Mater. Sci. Technol.*, 2020, **49**, 144–156.

174 R. B. Levy and M. Boudart, *Science*, 1973, **181**, 547–549.

175 L. H. Bennett, J. R. Cuthill, A. J. McAlister, N. E. Erickson and R. E. Watson, *Science*, 1974, **184**, 563–565.

176 A. Kumar Singh, C. Das and A. Indra, *Coord. Chem. Rev.*, 2022, **465**, 214516.

177 R. Tong, Z. Sun, X. Wang, S. Wang and H. Pan, *J. Phys. Chem. C*, 2019, **123**, 26136–26144.

178 Y. Zou, D. Ma, D. Sun, S. Mao, C. He, Z. Wang, X. Ji and J.-W. Shi, *Appl. Surf. Sci.*, 2019, **473**, 91–101.

179 L.-f Hong, R.-t Guo, Y. Yuan, X.-y Ji, Z.-d Lin, Z.-s Li and W.-g Pan, *ChemSusChem*, 2021, **14**, 539–557.

180 K. He, J. Xie, Z. Yang, R. Shen, Y. Fang, S. Ma, X. Chen and X. Li, *Catal. Sci. Technol.*, 2017, **7**, 1193–1202.

181 M. Shao, Y. Shao, S. Ding, R. Tong, X. Zhong, L. Yao, W. F. Ip, B. Xu, X.-Q. Shi, Y.-Y. Sun, X. Wang and H. Pan, *ACS Sustainable Chem. Eng.*, 2019, **7**, 4220–4229.

182 Y. Li, Z. Dong and L. Jiao, *Adv. Energy Mater.*, 2020, **10**, 1902104.

183 J.-W. Shi, Y. Zou, L. Cheng, D. Ma, D. Sun, S. Mao, L. Sun, C. He and Z. Wang, *Chem. Eng. J.*, 2019, **378**, 122161.

184 L. Cheng, S. Xie, Y. Zou, D. Ma, D. Sun, Z. Li, Z. Wang and J.-W. Shi, *Int. J. Hydrogen Energy*, 2019, **44**, 4133–4142.

185 B. Li, W. Guo, X. F. Lu, Y. Hou, Z. Ding and S. Wang, *Mater. Rep.: Energy*, 2023, **3**, 100230.

186 X. Jiang, Q. Liu, C. Cheng, F. Xing, C. Chen and C. Huang, *Int. J. Hydrogen Energy*, 2021, **46**, 5197–5206.

187 J.-Q. Yan, W. Peng, S.-S. Zhang, D.-P. Lei and J.-H. Huang, *Int. J. Hydrogen Energy*, 2020, **45**, 16094–16104.

188 H. Zhou, R. Chen, C. Han, P. Wang, Z. Tong, B. Tan, Y. Huang and Z. Liu, *J. Colloid Interface Sci.*, 2022, **610**, 126–135.

189 C. Cheng, S. Zong, J. Shi, F. Xue, Y. Zhang, X. Guan, B. Zheng, J. Deng and L. Guo, *Appl. Catal., B*, 2020, **265**, 118620.

190 C. Jin, C. Xu, W. Chang, X. Ma, X. Hu, E. Liu and J. Fan, *J. Alloys Compd.*, 2019, **803**, 205–215.

191 Z. Li, Y. Ma, X. Hu, E. Liu and J. Fan, *Chin. J. Catal.*, 2019, **40**, 434–445.

192 B. Ma, X. Li, D. Li and K. Lin, *Appl. Catal., B*, 2019, **256**, 117865.

193 B. Ma, X. Wang, K. Lin, J. Li, Y. Liu, H. Zhan and W. Liu, *Int. J. Hydrogen Energy*, 2017, **42**, 18977–18984.

194 D. Zhan, J. Tian, Q. Fu, P. Liu, Y. Zhao, W. Liu, D. Li, Y. Huang and C. Han, *Appl. Surf. Sci.*, 2023, **641**, 158463.

195 X. Zhou, Y. Fang, X. Cai, S. Zhang, S. Yang, H. Wang, X. Zhong and Y. Fang, *ACS Appl. Mater. Interfaces*, 2020, **12**, 20579–20588.

196 S. Sun, Y.-C. Zhang, G. Shen, Y. Wang, X. Liu, Z. Duan, L. Pan, X. Zhang and J.-J. Zou, *Appl. Catal., B*, 2019, **243**, 253–261.

197 M. Shao, H. Chen, S. Hao, H. Liu, Y. Cao, Y. Zhao, J. Jin, H. Dang, Y. Meng, Y. Huo and L. Cui, *Appl. Surf. Sci.*, 2022, **577**, 151857.